MID-AMERICA TRANSPORTATION CENTER

Report # MATC-MS&T: 131-2

Final Report

WBS: 25-1121-0005-131-2

Sensor-Assisted Condition Evaluation of Steel and Prestressed Concrete Girder Bridges Subjected to Fire - Phase II

Genda Chen, PhD
Professor and Robert W. Abbett Distinguished Chair in Civil Engineering
Director, Center for Intelligent Infrastructure
Director, INSPIRE University Transportation Center
Associate Director, Mid-America Transportation Center
Department of Civil, Architectural, and Environmental Engineering
Missouri University of Science and Technology

Yanping Zhu, PhD,
Postdoctoral Scholar
Department of Civil, Architectural, and
Environmental Engineering
Missouri University of Science and Technology

2023

A Cooperative Research Project sponsored by U.S. Department of Transportation- Office of the Assistant Secretary for Research and Technology

Sensor-Assisted Condition Evaluation of Steel and Prestressed Concrete Girder Bridges Subjected to Fire – Phase II

Yanping Zhu, Ph.D. Postdoctoral Scholar
Department of Civil, Architectural, and Environmental Engineering
Center for Intelligent Infrastructure
Missouri University of Science and Technology

Genda Chen, Ph.D., P.E., F. ASCE
Professor and Robert W. Abbett Distinguished Chair in Civil Engineering
Director, Center for Intelligent Infrastructure
Director, INSPIRE University Transportation Center
Associate Director, Mid-America Transportation Center
Department of Civil, Architectural, and Environmental Engineering
Missouri University of Science and Technology

A Report on Research Sponsored by

Mid-America Transportation Center

University of Nebraska–Lincoln

December 2023

Technical Report Documentation Page

1. Report No.
25-1121-0005-131-2

2. Government Accession No.

3. Recipient's Catalog No.

4. Title and Subtitle
Sensor-Assisted Condition Evaluation of Steel and Prestressed Concrete Girder Bridges Subjected to Fire – Phase II

5. Report Date
December 2023

6. Performing Organization Code

7. Author(s)
Yanping Zhu, and Genda Chen

8. Performing Organization Report No.
25-1121-0005-131-2

9. Performing Organization Name and Address
Center for Intelligent Infrastructure
Department of Civil, Architectural, and Environmental Engineering
Missouri University of Science and Technology
500 W. 16th Street
Rolla, MO 65409-0810

10. Work Unit No. (TRAIS)

11. Contract or Grant No.
69A3551747107

12. Sponsoring Agency Name and Address
Mid-America Transportation Center
2200 Vine St
PO Box 830851
Lincoln, NE 68583-0851

13. Type of Report and Period Covered
Final Report
January 1, 2019 – March 30, 2023

14. Sponsoring Agency Code
MATC TRB RiP No. 91994-28

15. Supplementary Notes

16. Abstract

This report summarizes the results and findings of Mid-America Transportation Research Center (MATC) research project No. 57768. In this study, fire dynamics simulation (FDS) is conducted on a new Pyrosim software platform and validated experimentally to understand the surrounding air temperature and internal temperature of reinforced concrete (RC) beams under channel fires fueled by natural gas, which is released from four burners in a controllable fashion. For statistical analysis, four RC beams were designed, cast, and tested. Heat release rate (HRR) was measured and used as the fire load input to each test beam. The effects of mesh size, computational zone, side hole area, and burner surface temperature were investigated through parametric analysis. The predicted air temperatures from a FDS model compared well with the experimental results with a maximum difference of 20% for both maximum and average temperatures of the beams when loaded at a constant HRR. Even one-dimensional heat conduction in the FDS satisfactorily predicted the internal temperature of beams on the fire side and bounded the experimental temperatures after the predicted temperatures conducted from different surfaces were superposed. The effects of concrete specific heat, thermal conductivity, and wind gust were investigated numerically.

17. ORCID No. of each Researcher
Genda Chen: 0000-0002-0658-4356

18. Distribution Statement

19. Security Classif. (of this report)
Unclassified

20. Security Classif. (of this page)
Unclassified

21. No. of Pages
66

22. Price

Table of Contents

List of Figures

List of Tables

Acknowledgments

Financial support was provided by Mid-America Transportation Research Center under contract agreement No. 59709. Thanks are due to Dr. Yi Bao, for his assistance to obtain test data of the small-scale concrete beams. The concrete beams were cast and tested by research staff in the National Fire Laboratory at National Institute of Standards and Technology under the leadership of Lisa Choe and Matthew S. Hoehler.

Disclaimer

Abstract

In this study, fire dynamics simulation (FDS) is conducted on a new Pyrosim software platform and validated experimentally to understand the surrounding air temperature and internal temperature of reinforced concrete (RC) beams under channel fires fueled by natural gas, which is released from four burners in a controllable fashion. For statistical analysis, four RC beams were designed, cast, and tested. Heat release rate (HRR) was measured and used as the fire load input to each test beam. The effects of mesh size, computational zone, side hole area, and burner surface temperature were investigated through parametric analysis. The predicted air temperatures from a FDS model compared well with the experimental results with a maximum difference of 20% for both maximum and average temperatures of the beams when loaded at a constant HRR. Even one-dimensional heat conduction in the FDS satisfactorily predicted the internal temperature of beams on the fire side and bounded the experimental temperatures after the predicted temperatures conducted from different surfaces were superposed. The effects of concrete specific heat, thermal conductivity, and wind gust were investigated numerically.

Chapter 1 Introduction

Fire safety research often requires multidisciplinary efforts from chemical engineering, civil engineering, mechanical engineering, and mathematics since the chemical and physical phenomena behind a fire event around engineering structures is governed by the Navier-Stokes equations. For structural engineering, a mature numerical analysis framework has been developed to determine structural behavior under fire conditions in three steps (Quiel et al. 2015). First, gas temperatures (or adiabatic surface temperatures surrounding an object) are obtained from a fire model. Then, the temperatures on the surface and inside of structural components can be obtained from a heat transfer model. Finally, the structural and mechanical responses can be obtained from a structural model. Different approaches have been proposed to model fire in the first step. Simple fire models directly use fire curves or radiation heat fluxes to represent a fire, while complex fire models such as a fire dynamics simulator (FDS) can be built upon computational fluid dynamics (CFD). The complex FDS couples the CFD model with thermodynamics (i.e., fire-driven fluid flow). One software program for the FDS was written by project scientists of the Building and Fire Research Laboratory at the National Institute of Standards and Technology (NIST). The FDS program can calculate the gas temperature, velocity, pressure, density, and chemical composition in each grid cell at different time steps as well as calculate adiabatic surface temperature, various heat fluxes, and mass loss rate.

Dotreppe et al. (2005) used the evolution of air temperature over time based on the hydrocarbon curve in the Eurocode to describe the fire environment. They analyzed a tied steel arch bridge with a concrete deck and observed the decrease in temperature away from the fire source and along the bridge. Liu et al. (2012) conducted the thermal and structural behavior analysis of a steel girder with a partial concrete deck from the MacArthur Maze Bridge in

Oakland, CA, USA, which collapsed on April 29, 2007. A temperature-time curve in the Eurocode was assumed underneath the middle of the bridge. Kodur et al. (2013) simulated the thermal and structural response of a beam-slab assembly exposed to an ISO 834 fire. Their subsequent study (2013) also considered hydrocarbon fire, moderate design fire, and external design fire curves as fire loads to analyze the thermal and structural behavior of a steel-concrete assembly. Similarly, Payá-Zaforteza and Garlock (2012) compared two alternative fire curves (a hydrocarbon fire in the Eurocode and a railroad tanker collision fire) to investigate the fire response of a steel girder bridge. The hydrocarbon fire differs significantly from the tanker collision fire in terms of heating rate, intensity, and duration. The hydrocarbon fire has a high fire intensity that induces extremely high temperatures in a few seconds, while the simple fire curve representing fires resulting from events other than burning fuel and crashing vehicles considers a uniform heating.

Choi (2008) applied the FDS to first model the progression of a fire and then generated the spatiotemporal temperatures or heat fluxes on the surfaces of a steel-concrete structure in a discrete numerical form for a subsequent heat transfer analysis. Bajwa et al. (2012) applied the FDS to model the large open pool portion of the MacArthur Maze fire to obtain boundary fire temperatures, and the refined model with specific features of the fire yielded an upper uniform temperature limit of 1100 ℃. Wright et al. (2013) applied the FDS to predict the flame height, gas temperature, and heat flux, and imported the heat flux boundary condition to a finite element model to perform heat conduction and emissivity and predict the temperatures in the structural members of the I-65 Birmingham Bridge. Alos-Moya et al. (2014) created a fire model of the I-65 overpass in Birmingham, Alabama, USA, based on the CFD. The calculated adiabatic surface temperatures from the FDS were used to heat the bridge deck in the thermo-mechanical analysis using a finite element model. The heat release rate of the spilled fuel and discretization of the adiabatic surface temperature in the transition from the FDS to the finite element model were parametrically analyzed. Tonicello et al. (2012) used the FDS to simulate several realistic fire scenarios, and the adiabatic gas temperatures on the simplified representation of the real structure were obtained and used as input for the SAFIR heating calculation.

The complex FDS-based fire models provide a practical spatiotemporal variation of temperatures, such as adiabatic surface temperature, which is an intermediate quantity in heat transfer analysis following structural analysis in a thermo-mechanical model. Alos-Moya et al. (2019) used the measured temperatures of the Valencia bridge during fire tests to calibrate the simple fire models (with analytical temperature equations) established by a Heskestad and Hamada's correlation curve and the advanced CFD models used in the FDS. The FDS provided satisfactory temperature predictions in the analysis of the real bridge fires. However, the noted effect of winds during these fire tests in the open air was not taken into consideration. As a result, the average temperatures obtained numerically during the fire plateau stage were 30-120% higher than those obtained during the experiments. Although the layer thicknesses and material properties of the bridge were included in the FDS for one-dimensional heat conduction analysis, no results were reported in their study. Timilsina et al. (2021) conducted the post-fire analysis of a fire-damaged concrete bridge based on the CFD. The fire modeling, heat transfer analysis, and stress analysis of the bridge were performed. The surface temperature time histories obtained from the fire model along the traffic directions of all girders were used as input in heat transfer analysis. However, the concrete elastic modulus was updated manually to calibrate the stress analysis model until the finite element deflections and strains matched with the test results. Represented by its uniform speed and preset direction (Peris-Sayol et al. 2015, Dréan et al.

2022), the wind was simply introduced as a boundary condition on the windward side of the model or computational domain. The wind speed over the height of the domain was assumed to be unchanged with time. Therefore, the FDS-based fire model is yet to be validated in a realistic setting using physical experiments.

In this study, fire dynamics simulations are conducted on a new Pyrosim software platform and validated experimentally to understand the surrounding air temperature and internal temperature of reinforced concrete (RC) beams and enhance the understanding of controllable parameters when implementing the FDS tool. Four RC beams were designed, cast, and tested under channel fires fueled by natural gas, which is released from four burners in a controllable fashion. The heat release rate (HRR) was measured and used as the fire load input to each test beam. The effects of mesh size, computational zone, side hole area, and burner surface temperature were investigated through parametric analysis. The present study sheds new insights into the FDS modeling technique in several ways. First, the effects of various parameters on gas temperature were clarified. Second, the influences of potential parameters in one-dimensional heat conduction of the concrete beams were revealed. The obtained adiabatic surface temperature distribution can be used in heat transfer analysis through a finite element model. Third, the effect of wind was considered in the FDS through the Monin-Obukhov similarity theory.

Chapter 2 Experimental Description

Four small-scale RC beams were tested in a gas fueled compartment fire at NIST by Bao et al. (2017). These beams were instrumented with distributed fiber optic sensors and thermocouples and exposed to fires of increasing intensity. Since the measured temperatures will be compared to calculated temperatures in this study, the experimental details relevant to the FDS validation are described here, while other information such as specimen preparation refers to the previous publication (Bao et al. 2017). Additional information on the fire test setup was obtained through personal communication with Mr. Matthew S. Hoehler—a research engineer in the National Fire Laboratory at NIST.

Figure 2.1(a) shows an overview of the test setup. It includes a burner rack, an enclosure above the rack, and water-cooled pipe supports for a test specimen inside the enclosure. The enclosure is formed by two side walls, two end walls, and a top cover. In a schematic view of the test setup as shown in Figure 2.1(b), the distance between two pipe supports rested on masonry blocks measured 49.2 in. The top of the water-cooled pipes is 52.5 in. above the ground.

Figure 2.2(a) shows a specific design of the flame channel that is made of cold-formed steel C-channels, a 1/2-in.-thick gypsum board lined with a refractory fiber board, 1/2-in.-thick 2-ply kaowool boards, and a 1-in.-diameter square steel tube. Each side wall of the flame channel was 15 in. (vertical) plus 8 in. (vertical when projected from an approximately 45° inclined board) high. The two vertical side walls were 16 in. apart. The flame channel was 72 in. in length and 39 in. above the ground. Figure 2.2(b) shows the dimensions of a water-cooled support assembled from a 1-1/2-in. schedule 40 steel pipe with an outer diameter of 1.9 in., 3/4-in. garden hose fitting, and two box sections. Therefore, the enclosure created a heated area of 15 in.

× 16 in. × 72 in. (height × width × length) and the bottom of the enclosure (flame channel) was open.

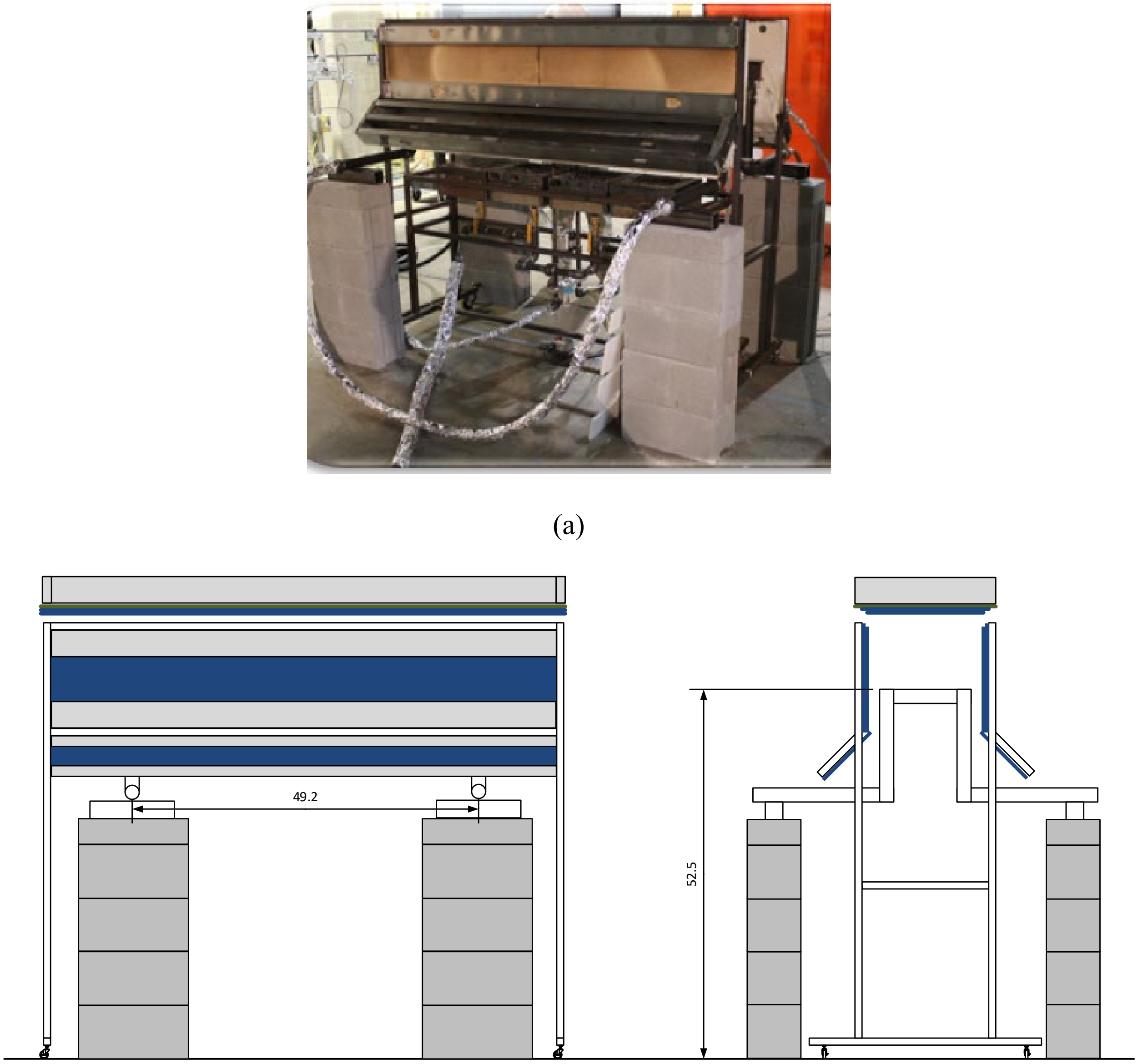

(a)

(b)

Figure 2.1 (a) Overview of the flame channel (b) Schematic view (unit: in, 1 in = 2.54 cm).

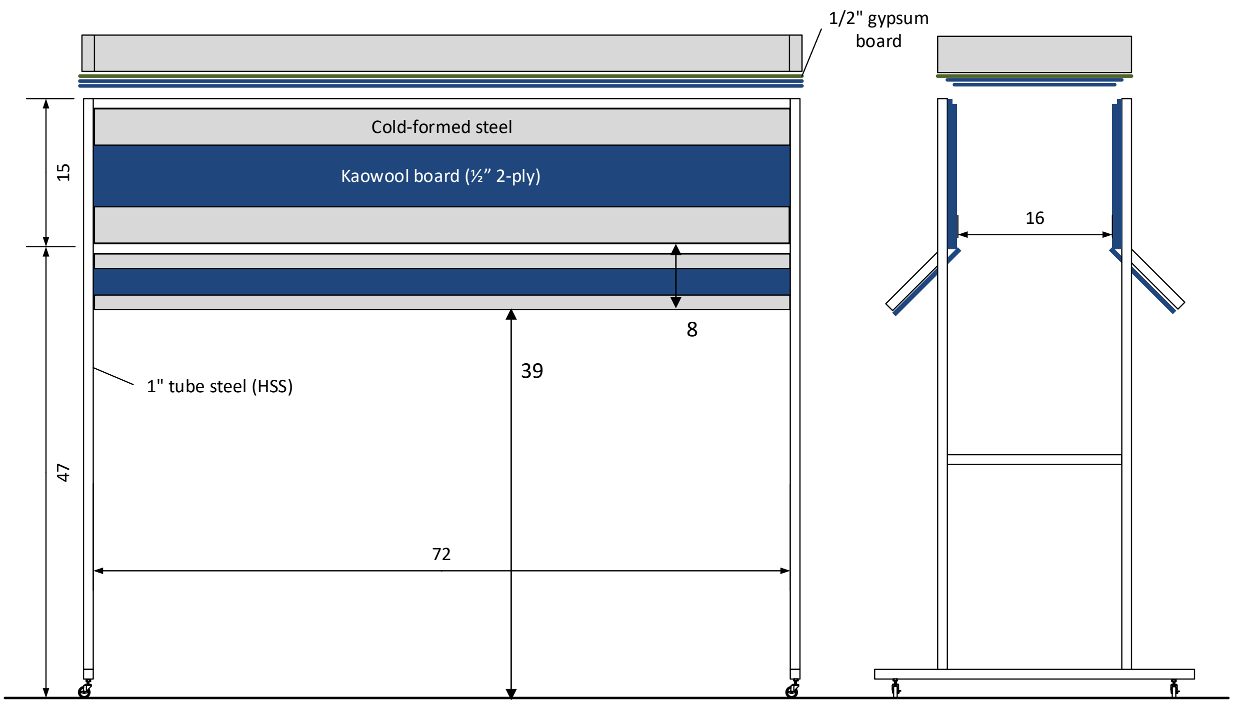

(a)

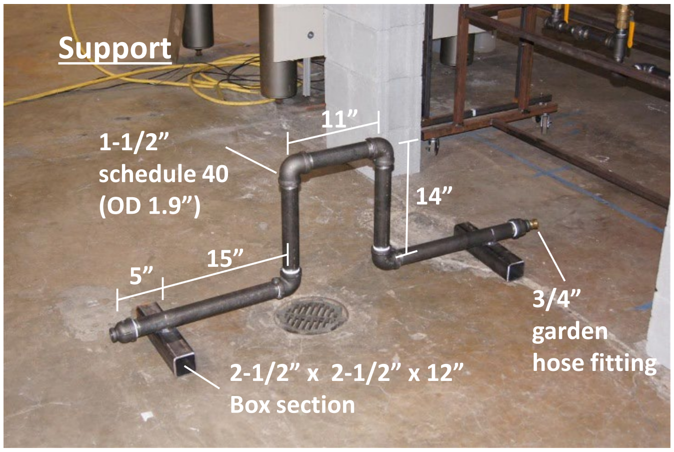

(b)

Figure 2.2 (a) Specific design of the flame channel (b) water-cooled support pipe (unit: in, 1 in = 2.54 cm).

The rack supported four independent natural gas diffusion burners made of sheet metal, each with dimensions of 12 in. × 12 in. × 5.5 in. (length × width × height) as shown in Figure

2.3. A needle valve on the gas line was used to regulate the gas supply. During each test, the two middle burners were fueled with natural gas from their bottom through the burner cavity and a 20 mm thick ceramic fiber blanket for gas distribution. Figure 2.4(a) shows the locations of five glass sheathed, K-type bare-bead thermocouples (TC-chan-1 to TC-chan-5) for measuring air temperature in the flame channel. The gas temperature thermocouples were deployed at the mid-height of the side wall spaced at 12 in. center-to-center. The thermocouple beads were extended approximately one inch into the flame channel from the side wall. Figure 2.4(b) shows four glass sheathed, K-type bare-bead thermocouples (TC1, TC2, TC3 and TC4) embedded in each concrete beam. TC1 was deployed at the quarter span and one-half depth of the concrete beam, while TC2, TC3, and TC4 were at the mid-span and 1/4, 1/2, and 3/4 depths of the concrete beam, respectively.

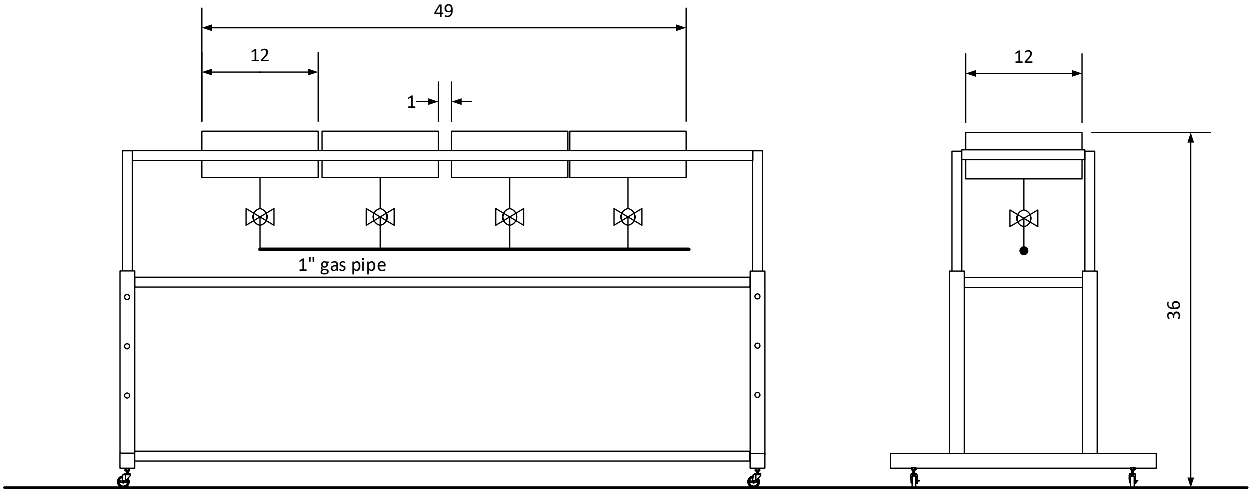

Figure 2.3 Burner rack dimensions (unit: in, 1 in = 2.54 cm).

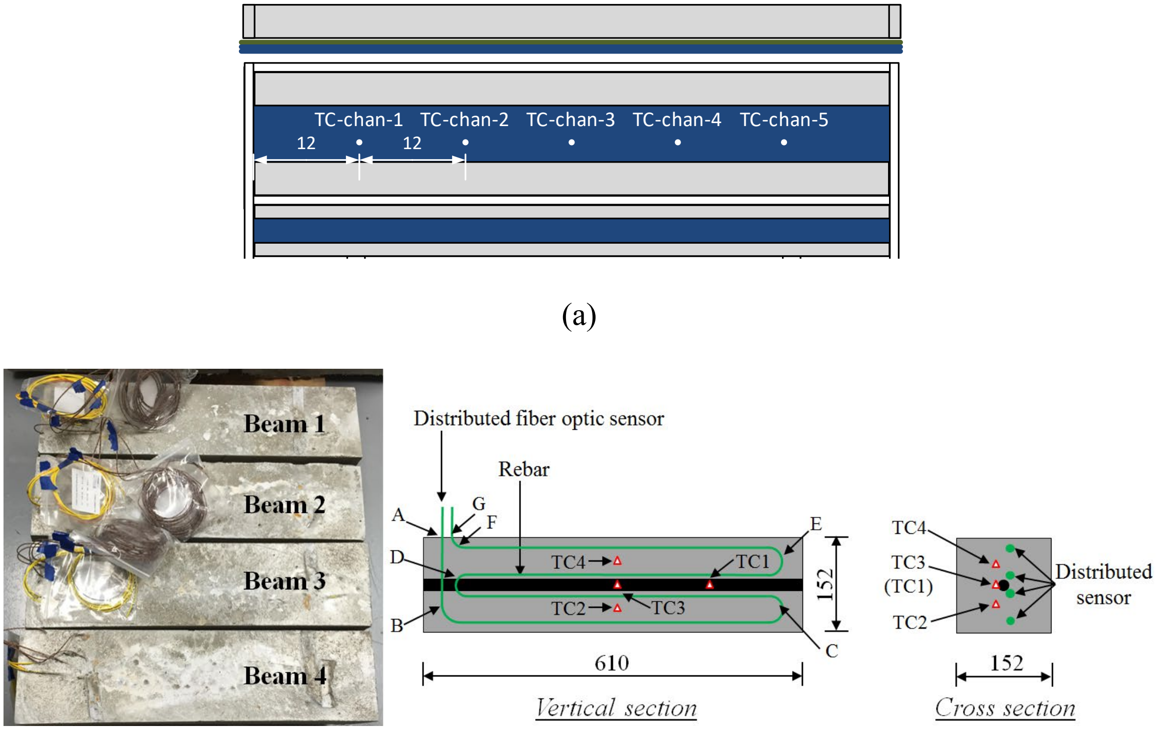

(a)

(b)

Figure 2.4 Instrumentation plan: (a) thermocouples on the inner face of a side wall of the flame channel and (b) thermocouples embedded in concrete beams Bao et al. (2017) (unit: mm).

HRR is a characteristic variable used to measure a fire in fire engineering. The burner HRR was controlled at different intensities to fire concrete beams. Table 2.1 shows the durations of each stage at a sustained HRR value for the four concrete beams. Figure 2.5 shows the test protocols of the concrete beams in terms of HRR (kW) and average compartment air temperature (°C) curves at different stages over time (min). They can be used in the FDS and for model validation, respectively. Note that Beam 1 and Beam 2 had nearly the same protocol.

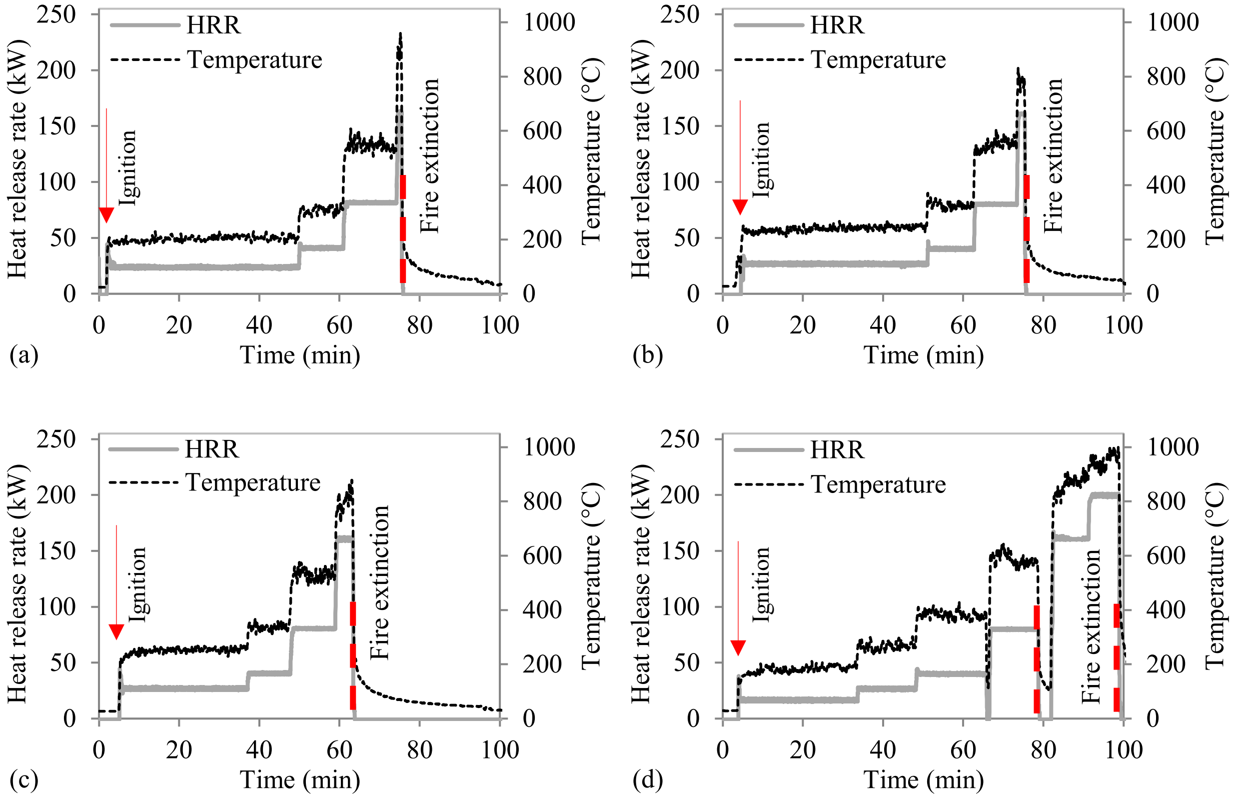

Figure 2.5 HRR and average compartment air temperature protocols for: (a) Beam 1, (b) Beam 2, (c) Beam 3, and (d) Beam 4 (extracted from Bao et al. (2017)).

Table 2.1 Durations of each sustained heat release rate (HRR) value for concrete beams.

HRR (kW)	Duration (min)			
	Beam 1	Beam 2	Beam 3	Beam 4
15	N/A	N/A	N/A	30
25	45	45	30	15
40	10	10	10	10
80	10	10	10	10
160	1	2	4	10
200	N/A	N/A	N/A	8

Chapter 3 Computational Fluid Dynamics (CFD) Model and Simulations

3.1 Introduction

An FDS implemented in the PyroSim software is used to predict the simulation results for the four RC beams tested previously at the NIST National Fire Laboratory. The FDS can establish a fire driven fluid flow model. The model numerically solves the Navier-Stokes equations at low speed when the Mach number is below 0.3 and thermally drives flow to capture smoke and heat transport in fire. An explicit predictor-corrector scheme as the core algorithm exhibits a second-order accuracy in time and space domains. A Large Eddy Simulation model is used for simulating any turbulence. In the combustion process, single-step and mix-controlled chemical reactions can be implemented in the FDS for three lumped species: fuel, air, and products. The fuel and products can be explicitly calculated. The radiation transport equation is solved using a finite volume method for a gray gas to include radiative heat transfer during a radiation transport. The RadCal narrow-band model in the FDS is used to compute gas-soot mixtures' absorption coefficients. In this study, the FDS model is further validated by the fire test results at NIST (Bao et al. 2017) in addition to the previous bridge tests (Paya-Zaforteza and Garlock 2012, Also-Moya et al. 2014, Also-Moya et al. 2019, Peris-Sayol et al. 2015, Gong and Agrawal 2017). The well-controlled fire tests in the NIST National Fire Laboratory for small RC beams at different HRR values are more insightful in validating the FDS than the fire tests of actual bridges.

An FDS model can be built in four steps. First, a control space is selected to represent a computational domain with boundary conditions. The control space is discretized into a grid of meshes. Second, a geometrical model established in the control space is subjected to a fire and the material properties of the remaining model, such as density, conductivity, specific heat absorption, and emissivity, are assigned to various meshes. Third, a fire source or load (natural gas in this study) is defined by an HRR value, and a combustion model is introduced. Fourth, sensing devices are deployed to output analysis results such as gas temperatures and internal beam temperatures. These steps are detailed as follows.

3.2 Control Space and Mesh

Figure 3.1 shows the control space used in the FDS. It includes the RC specimen and a required volume that exceeds nine times the specimen volume. Each side of the space is at least three times the specimen aspect. The entire space measures 1.83 m × 0.50 m × 0.66 m; it is defined and bounded in a xyz Cartesian coordinate system as $-0.915 \leq x \leq 0.915$ m, $-0.25 \leq y \leq 0.25$ m, and $-0.368 \leq z \leq 0.292$ m. For simplicity, the control space is evenly divided into a total of 4,070 parallelepiped cells with 37, 10, and 11 cells in the x, y, and z directions, respectively. Each cell thus measures 0.0495 m × 0.0500 m × 0.0600 m, corresponding to a maximum cell aspect ratio of 1.21, following the FDS user's guide version 6 in which it must be smaller than two. Since they affect calculation efficiency and accuracy, these mesh sizes are determined through a sensitivity analysis. Figure 3.1 shows the distribution of meshes in the control space. The vents for gas release are located at the bottom (i.e., Min z) and two side walls (i.e., Max y and Min y).

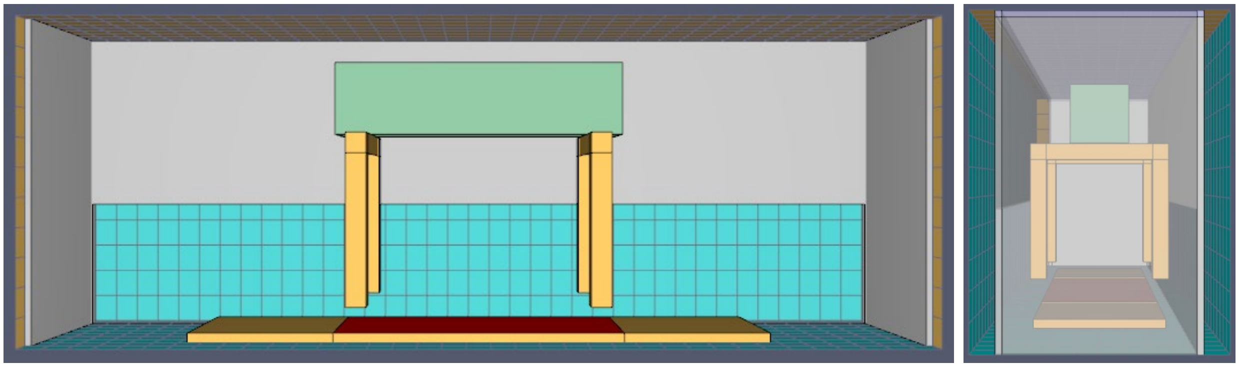

(a) (b)

Figure 3.1 Evenly distributed meshes in the control space of the FDS model: (a) front view and (b) right view.

3.3 Geometry and Materials

Each RC beam as shown in Figure 3.1 measures 0.610 m × 0.152 m × 0.152 m (length × width × height). The steel rebar is ignored in this study to avoid any complication to establish circle and inclined shape obstructions in the FDS. By defining layer thicknesses and material properties of the beam, one-dimensional heat transfer calculation can be conducted in the FDS as discussed in detail later. Each of the two end walls measured 0.40 m × 0.66 m excluding the 0.05 m-wide gap on each side, while each of two side walls had a plan dimension of 1.83 m × 0.66 m. All the walls were 0.013 m thick. Two holes with a plan dimension of 1.83 m × 0.282 m each were created on the two side walls to simulate two side openings near the bottom of the control space. The height of the holes represents the gap (about 3 in.) between the burner rack and the bottom of the flame channel. The water-cooled steel pipes to support each concrete beam were simulated in the computational domain. The vertical tubes measured 0.042 m × 0.042 m × 0.356 m. The horizontal tubes have dimensions of 0.042 m × 0.042 m × 0.364 m. Note that these dimensions faithfully follow the dimension of the test setup in the practical test and some estimations are made to simplify model establishment.

Four square burners were supported on the rack in a row and prepared to generate a gas fueled fire. Each burner measured 300 mm × 300 mm (length × width) and was covered with a 20-mm-thick ceramic fiber blanket for gas distribution. During this study, only the two middle burners were lit and the other two burners were used as obstructions that would affect the fire-driven fluid flow beneath the flame channel. Three mesh boundary vents were created at the two side walls and the bottom of the flame channel to simulate air exchanges. The outside of the top cover and the bottom burner rack as well as the outside of the two end walls were in contact with computing meshing boundaries. Note that each side wall was kept 0.05 m apart from its nearby mesh vent to ensure that the opening was away from holes to avoid simulation terminations. For the walls and water-cooled beam supports, inert surfaces were assigned since they are subject to the ambient temperature. The inert surfaces were also assigned to the two end burners. For concrete beams, layered surfaces were assigned so that the effect of different parameters on one-dimensional conduction can be investigated as will be discussed in Section 5.5. The height of the concrete beam was set to 0.152 m during calibration for gas temperature, which includes the thermal properties of the beam as listed in Table 3.1. The backing parameters (i.e., temperature boundary conditions) for concrete obstruction surfaces were set to be “exposed” or “air-gapped (Alos-Moya et al. 2019), which will be discussed further in parametric studies.

Table 3.2 Thermal properties of steel and concrete materials

Materials	Density ρ (kg/m^3)	Specific heat c (kJ/kg°C)	Conductivity λ (W/m°C)	Emissivity ε_m	Absorption coefficient
Concrete	2280	1.04	1.8	0.9	5.10^4
Steel	7850	0.46	45.8	0.95	5.10^4

3.4 Fire Load

Natural gas (i.e., methane, CH_4) is used to fuel a fire whose load on the concrete beam is represented by a simple chemistry model (McGrattan et al. 2013a, McGrattan et al. 2013b). The methane reaction is available in the Pyrosim fuel library (Thunderhead Engineering 2022). The critical flame temperature is 1,427 ℃ and the energy released per unit mass oxygen is 13,100 kJ/kg. Other parameters of the methane are selected as follows: a radiation factor of 0.35, a hydrogen factor of 0.1, and zero for CO yield, soot yield, and HCN yield.

The four fire protocols/scenarios as defined in Table 2.1 were studied in the FDS. The corresponding measured HRR values (total power during each fire test) as shown in Figure 3.1 were input into four fire models. The fire source was a horizontal rectangular surface of 0.3 m × 0.6 m from the two middle burners. The HRR per unit area, an input to the FDS model, was calculated by dividing the total HRR by the burner surface area. The purpose of using the HRR per unit area is to have a rapid ignition reaction in the FDS. For example, the maximum HRR for BEAM1 is 161.5 kW, and the HRR per area is equal to $161.5 \text{ kW} / (0.3 \times 0.6) \text{ m}^2 = 897.4 \text{ kW/m}^2$. A fixed temperature boundary condition model on the burner surface was introduced with an emissivity of 0.9 and a surface temperature of 300 ℃. This assumed surface temperature refers to the Pyrosim Tutorial.

3.5 Sensing Devices

Virtual sensing devices were deployed at strategic locations of the FDS to store desirable simulation data/results useful for any subsequent analysis and thus reduce the dimension/amount of output data/results. For example, five virtual thermocouples with a bead diameter of 1.0 mm were selected to obtain simulated gas temperatures that can be compared with those taken at the same locations from real thermocouples during fire experiments. The x, y, z coordinates of the four thermocouples embedded in each concrete beam were: (0, 0, 0.178), (0, 0, 0.102), (0, 0, 0.140), and (-0.1525, 0, 0.140). Gas temperatures can also be measured from gas-phase devices. Moreover, wall temperature, internal wall temperature, adiabatic surface temperature, and gas temperature at the solid surface can be defined through solid-phase devices in the FDS to record temperatures at different locations.

Chapter 4 Results and Discussion

In this section, all the results computed from the FDS model for four concrete beams are presented with some general remarks. A more detailed discussion about model uncertainties is given later to illustrate their effect on model accuracy.

4.1 BEAM1

The BEAM1 specimen was tested at a room temperature of 25.8℃ measured from an ambient thermocouple. Figure 4.1 compares the FDS-calculated HRR time history of BEAM1 with the measured HRR at 11 time instances used as input in the FDS model. As expected, the simulated time history locally matches well with the key measured data, which demonstrates confidence in the following fire simulations. Figure 4.2 shows a 3D plot of gas temperatures at 1500 s, 3200 s, 4000 s, and 4370 s, respectively. Each time represents one instance in each target plateau of the HRR curve in Figure 4.1. Figure 4.3 shows a 2D slice of gas temperatures across the vertical plane ($y = 0$ along the centerline of BEAM1). Figure 4.4 shows a 2D slice of velocity vectors across the vertical plane ($y = 0.1$ m). Figure 4.5 shows a 2D slice of velocity vectors across the vertical plane ($x = 0.025$ m perpendicular to the centerline of BEAM1). Figure 4.6 compares the simulated with the measured compartment air temperature. It can be observed from Figure 4.2 that the spatial distribution of gas temperatures is quite non-uniform at any instance or from one time to another. In particular, Figures 4.3 and 4.4 indicate that both the gas temperatures and the velocity vectors are asymmetrical about the vertical line at the mid-span of BEAM1 though the initial fire conditions at the beginning of the BEAM1 test is symmetric. Figure 4.5 also demonstrates that the velocity vectors are asymmetrical about the vertical line across the centerline of BEAM1. It is also seen from Figure 4.6 that the simulated compartment air temperatures at the locations of TC-chan-2, TC-chan-3, and TC-chan-5 compare well with the measured data at early stages. However, the comparisons at the locations of TC-chan-1 and TC-chan-4 are less satisfactory. The difference in these comparisons is also indicative of non-uniform temperature distributions in space.

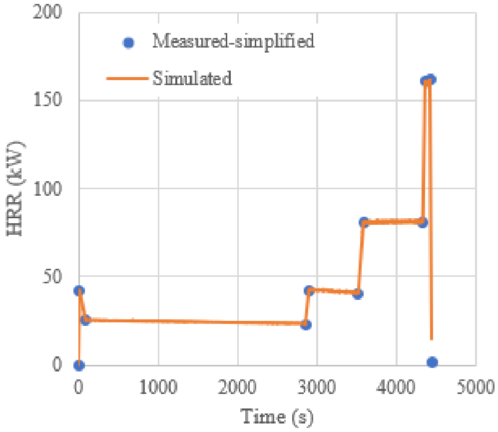

Figure 4.1 The simulated HRR time history versus the measured HRR values at 11 time instances: BEAM1.

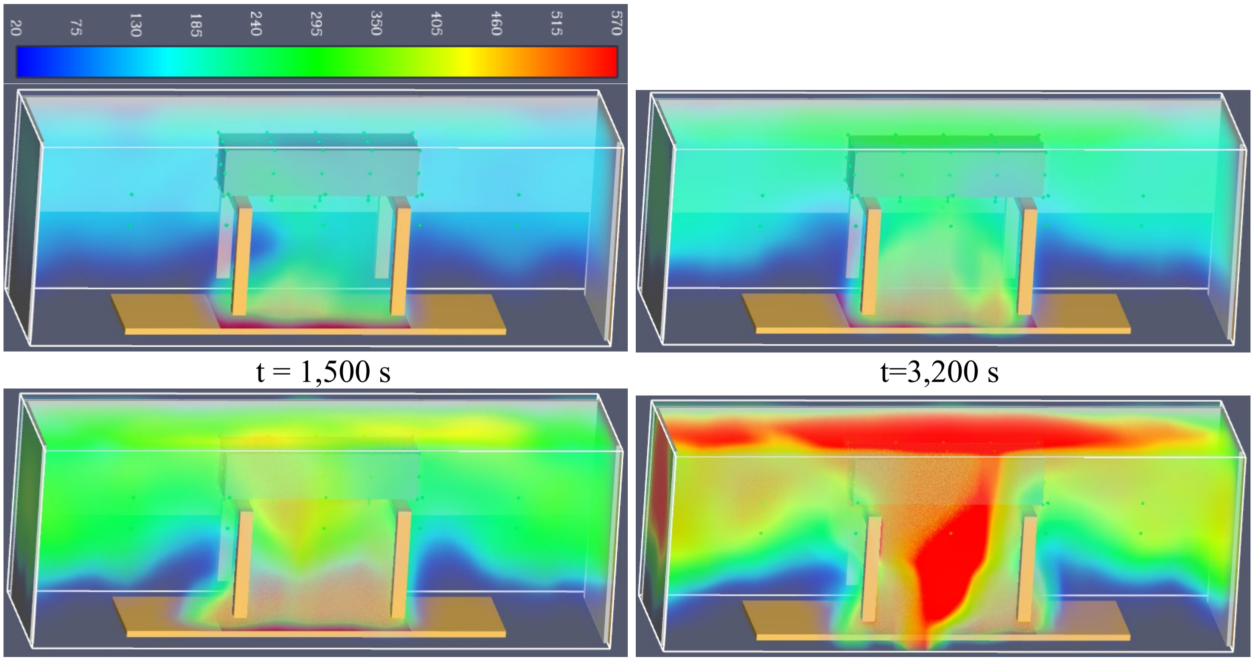

t = 1,500 s

t=3,200 s

t = 4,000 s

t = 4,370 s

Figure 4.2 3D plots of gas temperatures of BEAM1 at different times (unit: °C and green dots: virtual sensor locations).

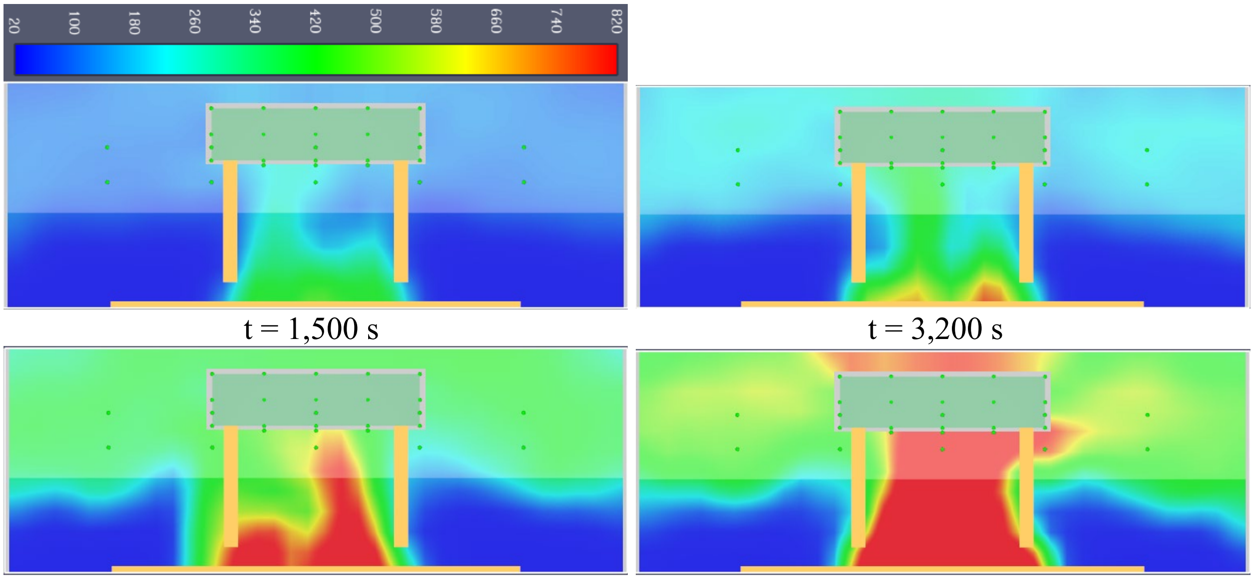

t = 1,500 s

t = 3,200 s

t = 4,000 s

t = 4,370 s

Figure 4.3 2D slices across the vertical plane (y = 0 and along the centerline) of BEAM1 at different times (unit: °C).

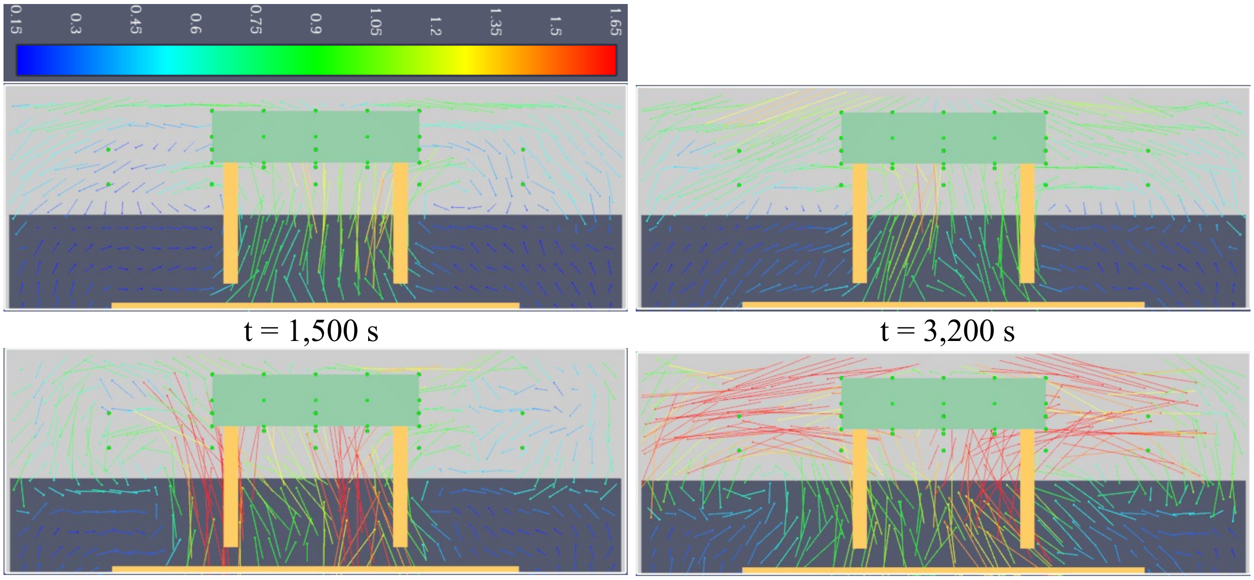

t = 1,500 s

t = 3,200 s

t = 4,000 s

t = 4,370 s

Figure 4.4 2D slices of velocity vectors across the vertical plane (y = 0.1 m) of BEAM1 at different times (unit: m/s).

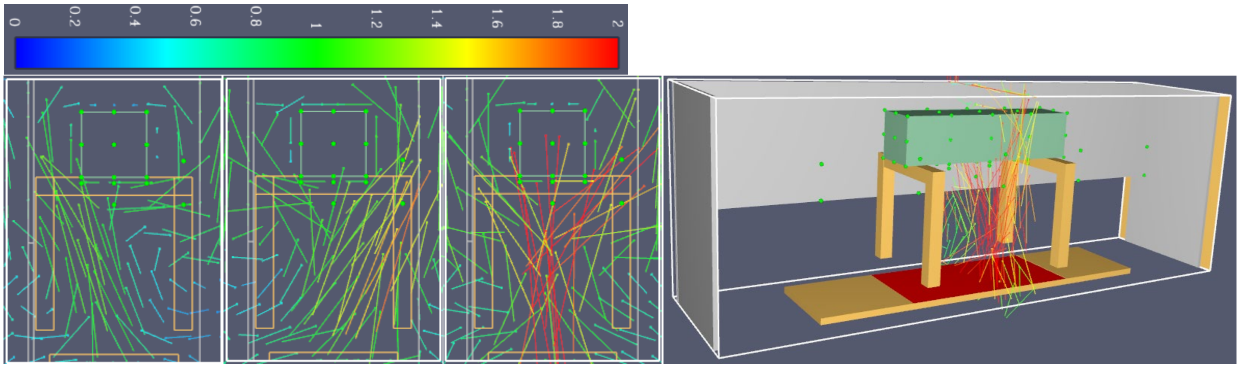

t = 1,500 s t = 3,200 s t = 4,000 s t = 4,370 s

Figure 4.5 2D slices of velocity vectors across the vertical plane (x = 0.025 m and perpendicular to the centerline) of BEAM1 at different times (unit: m/s).

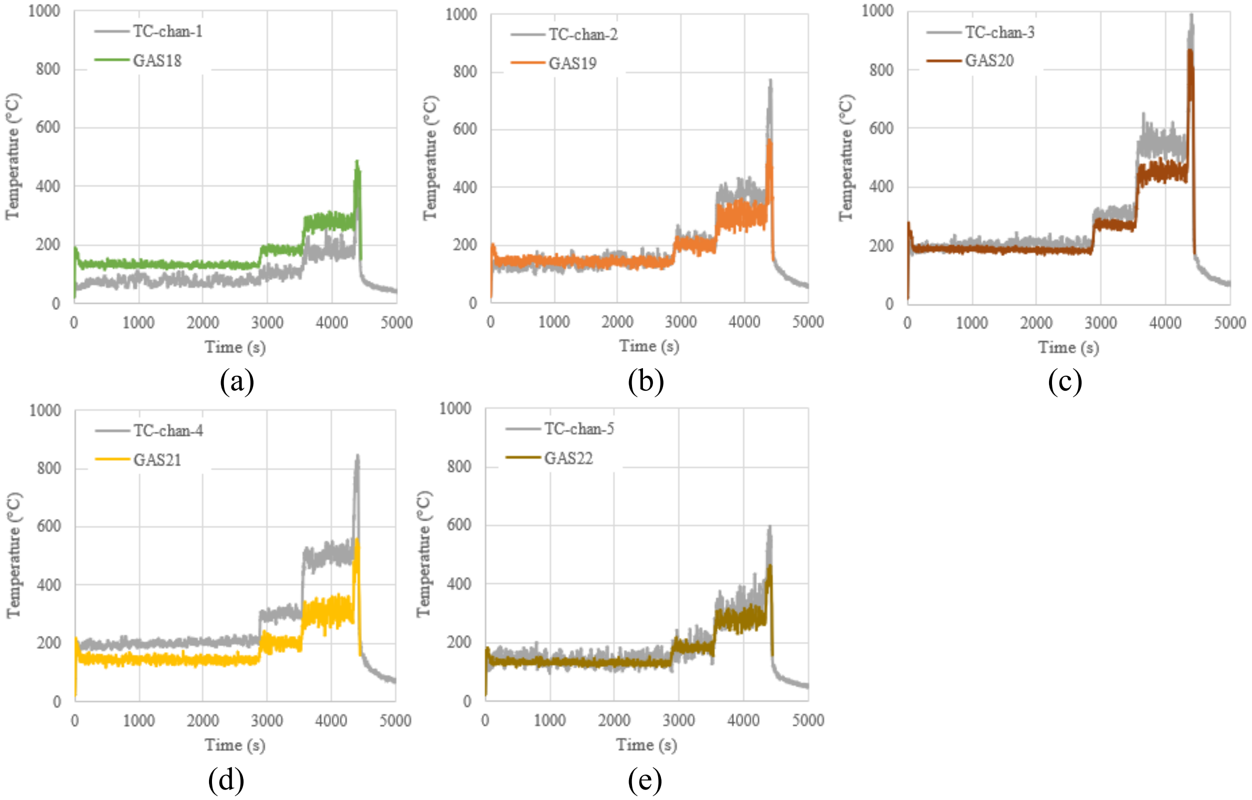

Figure 4.6 Simulated versus measured compartment air temperature during the BEAM1 test.

4.2 BEAM2

The BEAM2 specimen was tested with an initial compartment air temperature of 58.8 ℃ recorded (in contrast to a room temperature of 20℃). The inconsistency between the air temperature and the first HRR peak was likely attributed to the response time delay of the HRR measuring device during this test. Like Figure 4.1, Figure 4.7 presents the measured HRR values at 15 time instances and the simulated HRR time history in the FDS based on the measured values. Figures 4.8 and 4.9 show the compartment air temperature time histories at the locations of five thermocouples when the recorded initial temperature, 20℃ or 58.8 ℃, is considered corresponding to the initial HRR peak. As shown in Figure 4.8, the first case without including the initial temperature and HRR value gives rise to notable disparity between the simulated and the measured air temperatures at all five locations. As shown in Figure 4.9, the second case with the initial temperature and HRR value taken into account closes the comparison gap at the three thermocouple locations of TC-chan-2, TC-chan-3, and TC-chan-4. Therefore, the initial air temperature of 58.8 ℃ at the initial HRR peak is considered in all the following analyses except for internal beam temperatures since increasing an initial temperature inside the concrete in such a short time is not practical.

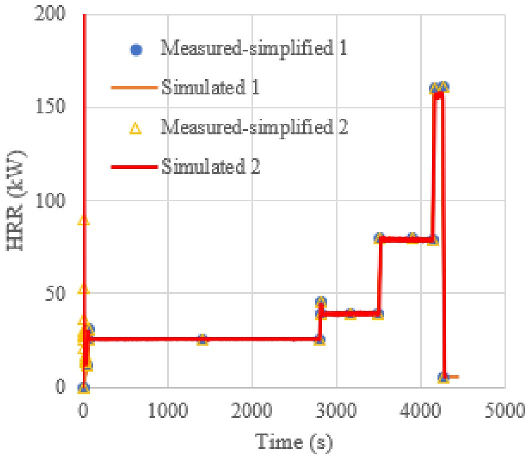

Figure 4.7 The simulated HRR time history versus the measured HRR values at 15 time instances: BEAM2.

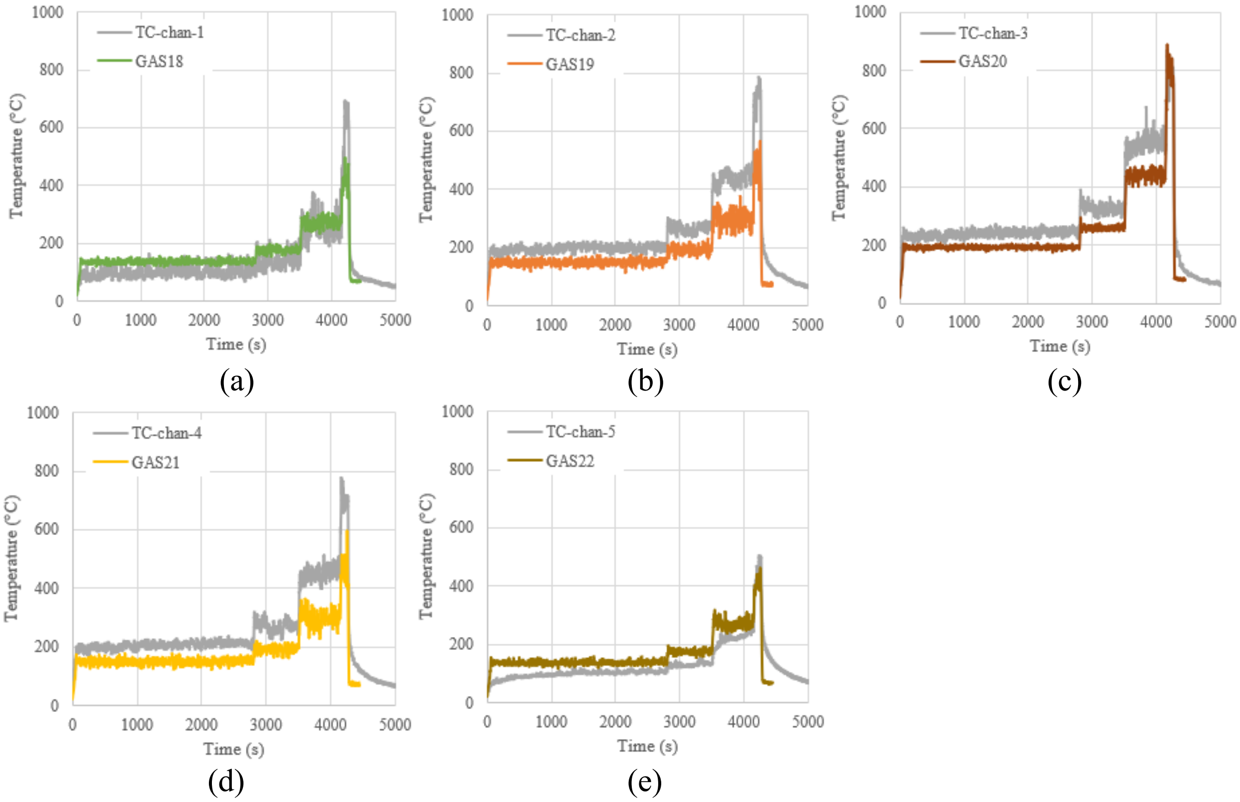

Figure 4.8 Simulated versus measured compartment air temperature during the BEAM2 test when an ambient computing temperature of 20℃ was considered at the initial HRR peak.

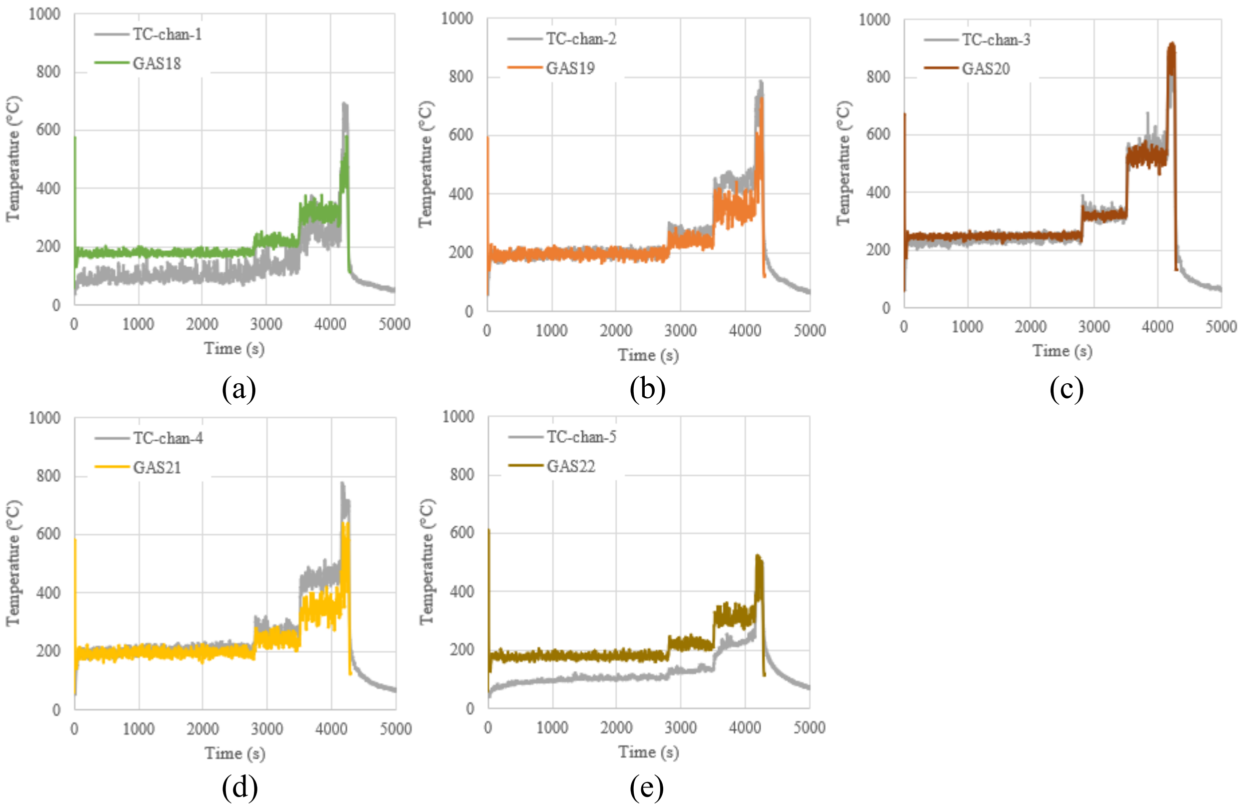

Figure 4.9 Simulated versus measured compartment air temperature during the BEAM2 test when an ambient computing temperature of 58.8℃ was considered at the initial HRR peak.

4.3 BEAM3

Figures 4.11 and 4.12 compare the air temperatures from the test and model of BEAM3. A comparison is made between the entire measured HRR curve and its simplified, measured HRR curve with 16 representative points over the test duration, as illustrated in Figure 2.5, as input for the FDS. It is found that the simplified, measured HRR curve can achieve the same modeling temperature accuracy as the entire measured HRR curve but save significant computational times. Therefore, the simplified HRR curve is used in the FDS of BEAM3.

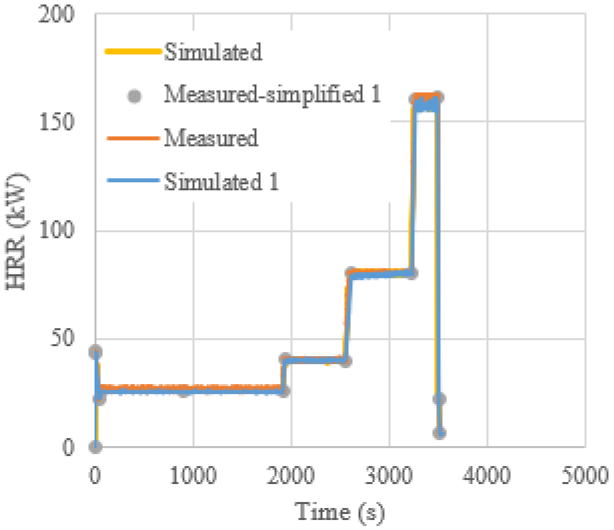

Figure 4.10 Comparison of the simplified measured HRR at 16 time instances and FDS simulated HRR: BEAM3.

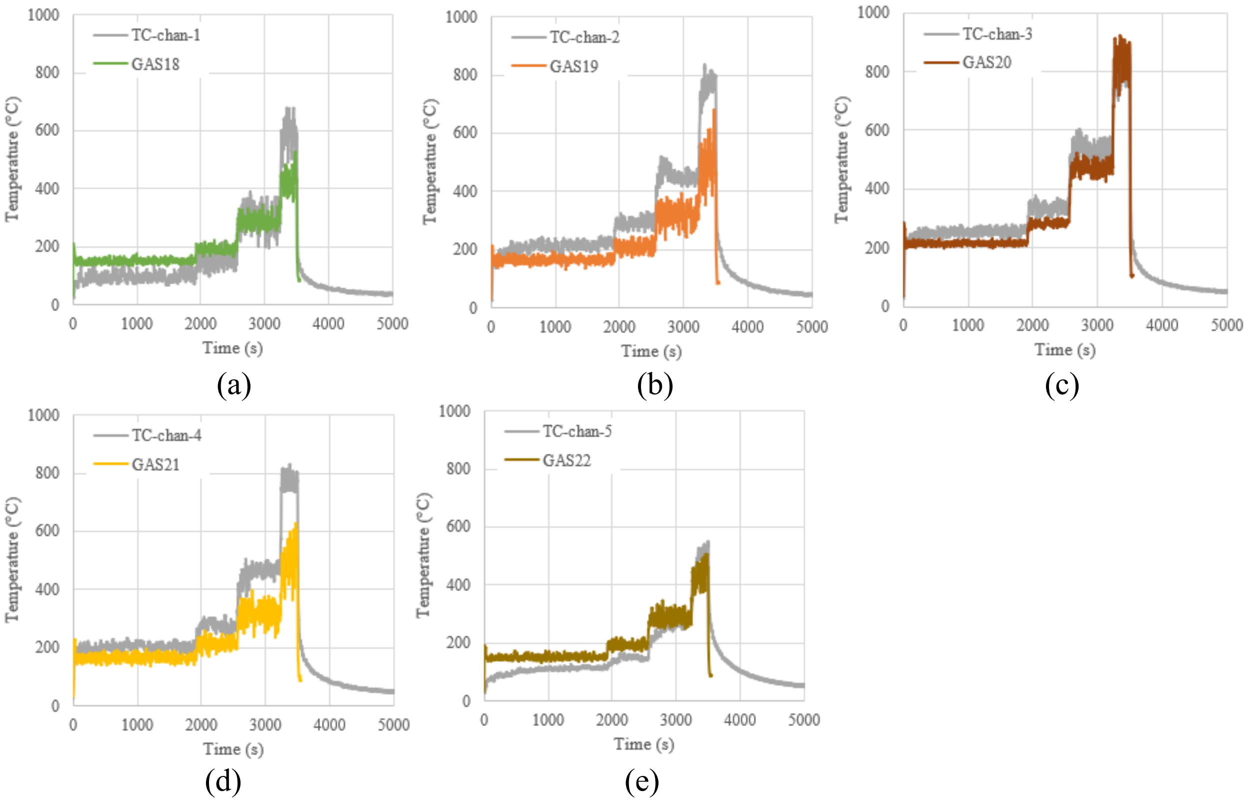

(a) (b) (c)

(d) (e)

Figure 4.11 Numerical and measured air compartment temperature: BEAM3 (Ambient computing temperature: 32.2℃ and no simplification for HRR).

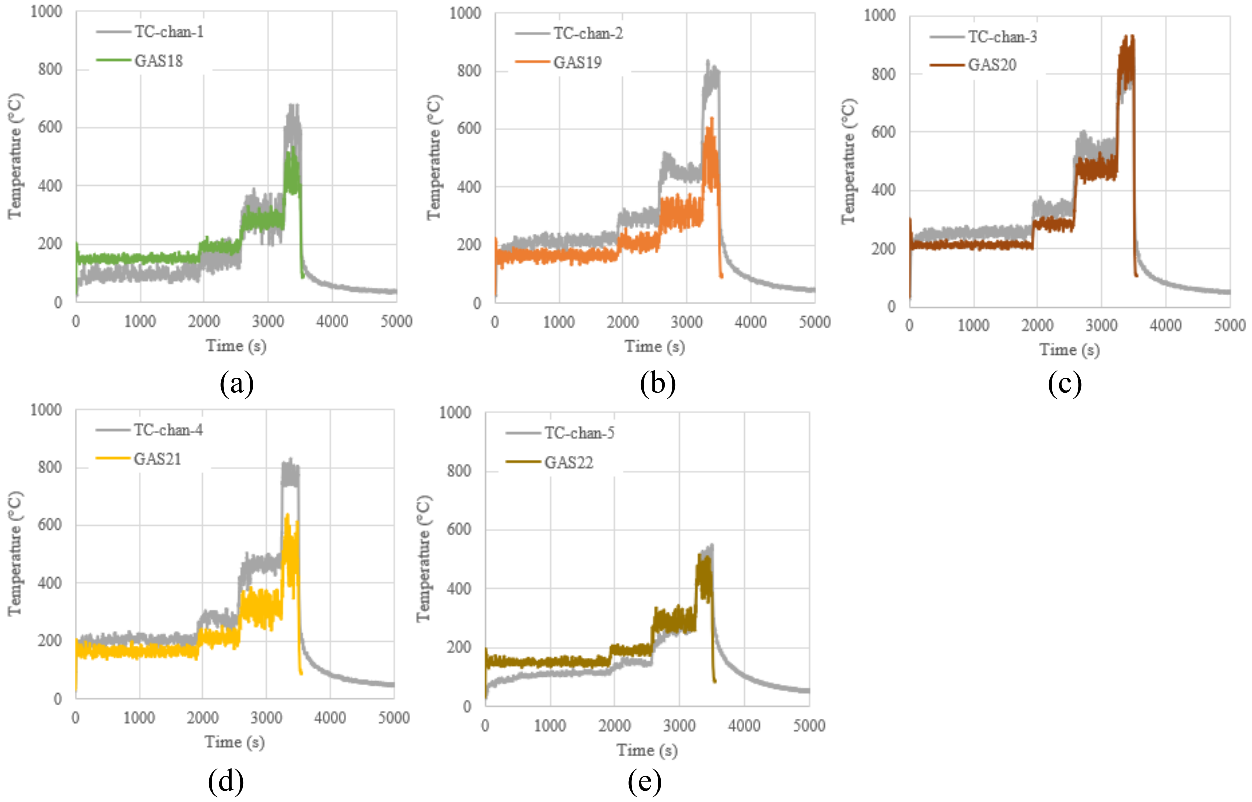

(a) (b) (c)

(d) (e)

Figure 4.12 Numerical and measured air compartment temperature: BEAM3 (Ambient computing temperature: 32.2℃ and simplified HRR).

4.4 BEAM4

For a comparison with BEAM3, the entire measured HRR is used for the modeling of BEAM4 as shown in Figure 4.13. Figure 4.14(b) is an FDS simulation result of HRRPUV in the mesh area at time of 5261.7 s and the heat release from the fire and the flame from the FDS are compared to the test observation when the beam was engulfed in fire (Figure 4.14(a)). Good agreement between them can be concluded from the flame appearance.

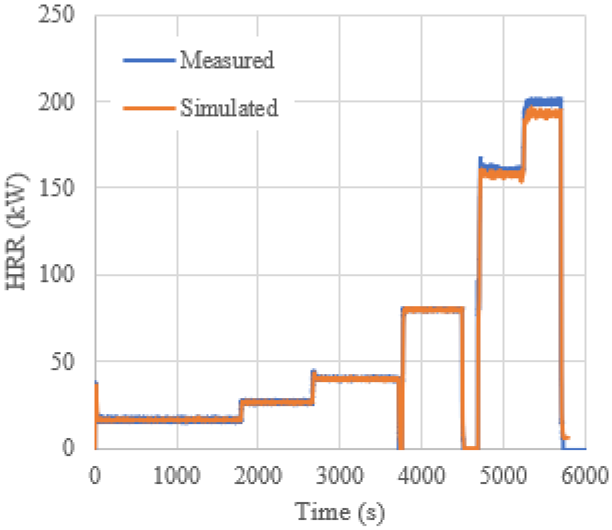

Figure 4.13 Comparison of the entire measured and FDS simulated HRR: BEAM4.


(a) (b)

Figure 4.14 (a) Visual inspection from the end view of BEAM4 when engulfed in fire illuminated by blue light to improve visualization (b) FDS simulation reuslt of HRRPUV in the mesh area at time of 5261.7 s.

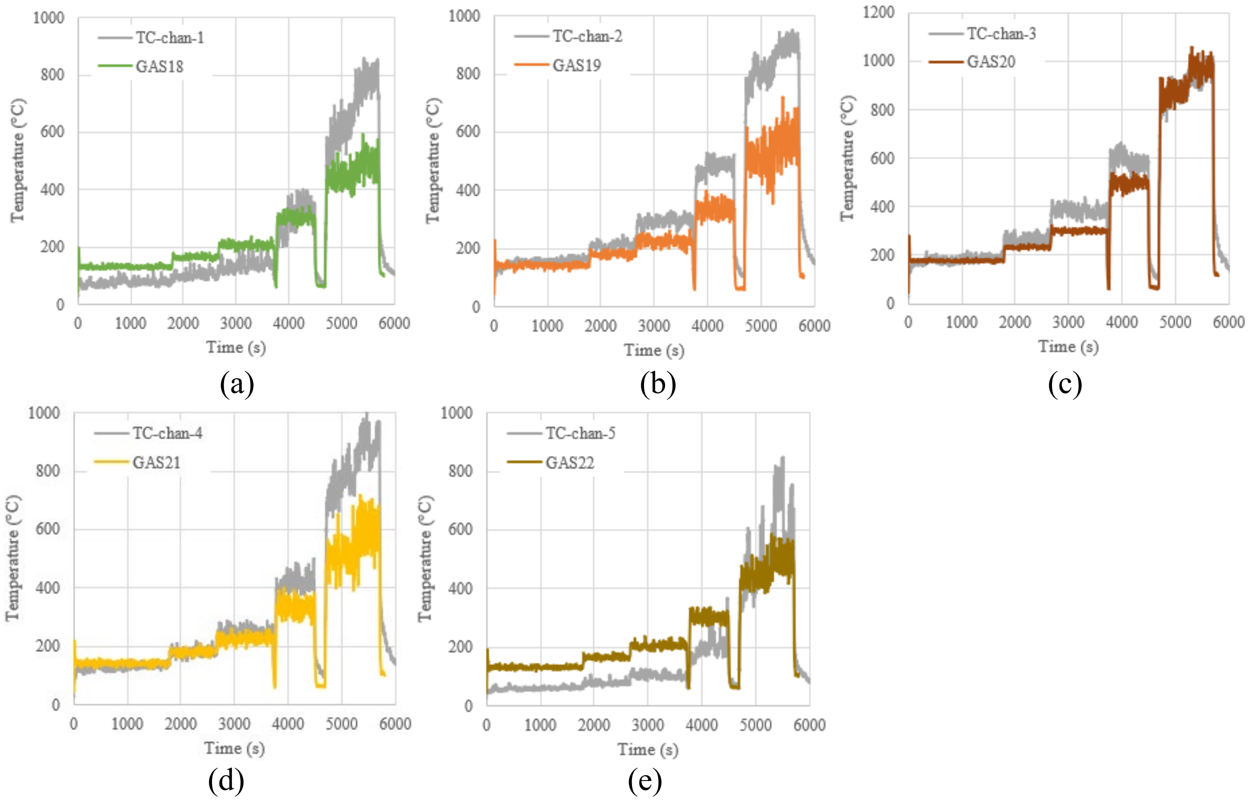

(a) (b) (c)

(d) (e)

Figure 4.15 Numerical and measured air compartment temperature: BEAM4 (Ambient computing temperature: 43.6℃ and no simplification for HRR.)

Chapter 5 Statistics for Comparison between Experimental and Numerical Results

5.1 Maximum, Minimum and Average Comparisons

From Table 2.1, there are four target HRR (i.e., plateau stage) for BEAM1, BEAM2, and BEAM3, and six target HRR for BEAM4. The time sustained for each target HRR of each beam during the test is determinable. Therefore, the maximum, minimum, and average temperatures during the sustained time of each HRR of the four beams can be extracted for the numerical and experimental comparison to evaluate the numerical model. Tables 5.1, 5.2, and 5.3 listed maximum, minimum, and average temperatures from the test and model. These temperatures will be used in the uncertainty analysis. Moreover, the average and maximum temperatures for the four beams are visualized in Figures 5.1-5.4. Since the initial heat release peak in BEAM2 induces significantly greater air temperatures in the FDS than the test, these temperatures are excluded for comparison. In general, the distribution of the maximum and average gas temperatures is well simulated in the FDS compared to the experimental results. The central temperatures are higher than the two sides since the middle two burners were ignited, and the central temperatures are well simulated by the FDS. Compared to average temperatures, the differences between the test and model are (-39%) to (75%), (-27%) to (88%), (-35%) to (58%), and (-36%) to (120%) for BEAM1, BEAM2, BEAM3, and BEAM4, respectively. From maximum temperature comparison, the differences between the test and model are (-28%) to (70%), (-18%) to (69%), (-27%) to (56%), and (-30%) to (88%) for BEAM1, BEAM2, BEAM3, and BEAM4, respectively. Moreover, most differences range between -20% and 20% for both average temperature and maximum temperature, and these differences are acceptable in the experimental validation of FDS models.

Table 5.3 Average temperature (T) obtained from the FDS and experimental test. Average temperatures were calculated at each constant HRR.

Average T (℃)	Locations	15 kW	25 kW	40 kW	80 kW	160 kW	200 kW
BEAM1	GAS 18	NA	132/**75**	182/**104**	276/**178**	425/**333**	NA
	GAS 19	NA	145/**138**	201/**214**	304/**371**	483/**668**	NA
	GAS 20	NA	188/**202**	271/**308**	450/**546**	803/**902**	NA
	GAS 21	NA	144/**200**	202/**300**	304/**500**	490/**781**	NA
	GAS 22	NA	132/**144**	182/**185**	278/**318**	419/**520**	NA
Average T (℃)	Locations	15 kW	25 kW	40 kW	80 kW	160 kW	200 kW
BEAM2	GAS 18	NA	179/**102**	219/**142**	316/**260**	462/**595**	NA
	GAS 19	NA	196/**198**	242/**268**	355/**440**	534/**731**	NA
	GAS 20	NA	250/**239**	322/**326**	526/**548**	881/**788**	NA
	GAS 21	NA	196/**203**	242/**270**	349/**449**	529/**705**	NA
	GAS 22	NA	179/**95**	220/**129**	315/**220**	463/**451**	NA
Average T (℃)	Locations	15 kW	25 kW	40 kW	80 kW	160 kW	200 kW
BEAM3	GAS 18	NA	151/**95**	192/**154**	284/**296**	435/**585**	NA
	GAS 19	NA	165/**209**	210/**294**	311/**454**	495/**762**	NA
	GAS 20	NA	212/**250**	284/**338**	473/**530**	846/**804**	NA
	GAS 21	NA	165/**202**	210/**274**	316/**459**	499/**772**	NA
	GAS 22	NA	151/**102**	191/**144**	288/**251**	439/**491**	NA
Average T (℃)	Locations	15 kW	25 kW	40 kW	80 kW	160 kW	200 kW
BEAM4	GAS 18	131/**77**	165/**102**	206/**137**	301/**303**	440/**602**	494/**777**
	GAS 19	142/**154**	181/**212**	225/**294**	335/**480**	501/**795**	572/**900**
	GAS 20	177/**182**	233/**266**	301/**382**	497/**586**	875/**861**	973/**949**
	GAS 21	143/**130**	181/**179**	226/**251**	333/**417**	503/**752**	592/**894**
	GAS 22	131/**59**	165/**78**	205/**103**	302/**199**	438/**446**	502/**657**

Table 5.2 Maximum (Max) temperature (T) obtained from the FDS and experimental test. Max temperatures were extracted at each constant HRR.

Max T (°C)	Locations	15 kW	25 kW	40 kW	80 kW	160 kW	200 kW
BEAM1	GAS 18	NA	190/**111**	200/**136**	312/**178**	486/**333**	NA
	GAS 19	NA	203/**189**	230/**269**	361/**371**	566/**668**	NA
	GAS 20	NA	279/**245**	292/**345**	500/**546**	868/**902**	NA
	GAS 21	NA	218/**227**	242/**335**	369/**500**	557/**781**	NA
	GAS 22	NA	182/**200**	217/**259**	330/**318**	464/**520**	NA
Max T (°C)	Locations	15 kW	25 kW	40 kW	80 kW	160 kW	200 kW
BEAM2	GAS 18	NA	574/**166**	252/**218**	378/**388**	578/**693**	NA
	GAS 19	NA	590/**228**	285/**317**	442/**494**	728/**786**	NA
	GAS 20	NA	670/**273**	352/**392**	579/**676**	918/**873**	NA
	GAS 21	NA	579/**235**	284/**319**	420/**515**	639/**770**	NA
	GAS 22	NA	621/**121**	254/**150**	363/**269**	524/**503**	NA
Max T (°C)	Locations	15 kW	25 kW	40 kW	80 kW	160 kW	200 kW
BEAM3	GAS 18	NA	204/**157**	226/**223**	331/**392**	534/**679**	NA
	GAS 19	NA	224/**248**	259/**333**	376/**521**	639/**837**	NA
	GAS 20	NA	301/**279**	308/**377**	529/**605**	930/**895**	NA
	GAS 21	NA	205/**234**	251/**311**	386/**504**	635/**831**	NA
	GAS 22	NA	195/**125**	213/**164**	344/**283**	516/**541**	NA
Max T (°C)	Locations	15 kW	25 kW	40 kW	80 kW	160 kW	200 kW
BEAM4	GAS 18	146/**115**	183/**144**	236/**209**	343/**402**	527/**712**	595/**859**
	GAS 19	159/**183**	199/**248**	264/**330**	398/**529**	619/**879**	719/**952**
	GAS 20	188/**235**	248/**309**	324/**440**	542/**664**	937/**949**	1056/**1020**
	GAS 21	159/**156**	210/**218**	261/**289**	402/**501**	681/**894**	719/**1003**
	GAS 22	146/78	184/**106**	237/**128**	336/**369**	546/**681**	576/**849**

Table 5.3 Maximum (Max) temperature (T) obtained from the FDS and experimental test. Max temperatures were extracted at each constant HRR.

Min T (℃)	Locations	15 kW	25 kW	40 kW	80 kW	160 kW	200 kW
BEAM1	GAS 18	NA	115/**46**	164/**76**	239/**137**	328/**274**	NA
	GAS 19	NA	115/**80**	162/**177**	238/**313**	344/**522**	NA
	GAS 20	NA	168/**118**	250/**269**	401/**486**	696/**676**	NA
	GAS 21	NA	116/**133**	163/**265**	227/**441**	410/**653**	NA
	GAS 22	NA	115/**93**	161/**127**	230/**242**	370/**440**	NA
Min T (℃)	Locations	15 kW	25 kW	40 kW	80 kW	160 kW	200 kW
BEAM2	GAS 18	NA	131/**39**	192/**94**	270/**173**	388/**411**	NA
	GAS 19	NA	141/**58**	209/**236**	282/**380**	374/**634**	NA
	GAS 20	NA	174/**62**	298/**292**	464/**476**	808/**695**	NA
	GAS 21	NA	140/**50**	201/**224**	272/**394**	353/**659**	NA
	GAS 22	NA	126/**38**	199/**116**	272/**169**	371/**381**	NA
Min T (℃)	Locations	15 kW	25 kW	40 kW	80 kW	160 kW	200 kW
BEAM3	GAS 18	NA	112/**39**	164/**99**	245/**196**	361/**462**	NA
	GAS 19	NA	121/**61**	175/**261**	245/**413**	341/**670**	NA
	GAS 20	NA	195/**111**	258/**299**	425/**460**	730/**701**	NA
	GAS 21	NA	135/**103**	173/**232**	236/**376**	347/**734**	NA
	GAS 22	NA	116/**38**	172/**121**	251/**206**	354/**415**	NA
Min T (℃)	Locations	15 kW	25 kW	40 kW	80 kW	160 kW	200 kW
BEAM4	GAS 18	121/**54**	151/**78**	185/**103**	269/**193**	376/**444**	413/**659**
	GAS 19	118/**106**	158/**188**	184/**244**	282/**413**	358/**687**	458/**853**
	GAS 20	168/**131**	219/**224**	282/**336**	446/**479**	790/**699**	894/**880**
	GAS 21	123/**99**	160/**150**	191/**215**	275/**332**	394/**618**	413/**801**
	GAS 22	118/**43**	150/**65**	186/**85**	272/**134**	385/**322**	418/**502**

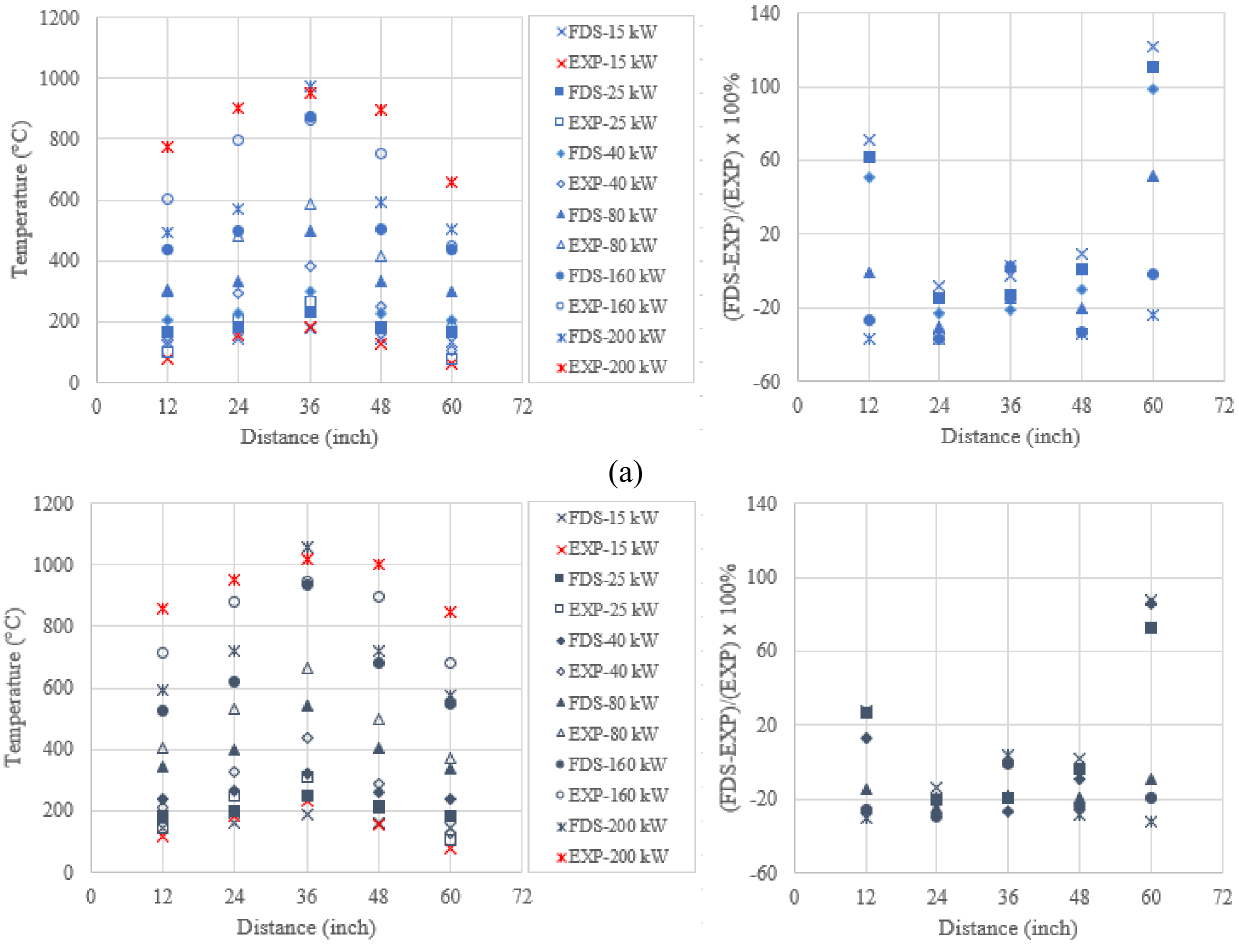

(a)

(b)

Figure 5.1 Comparison between experimental and numerical (a) average (b) maximum temperatures in BEAM4.

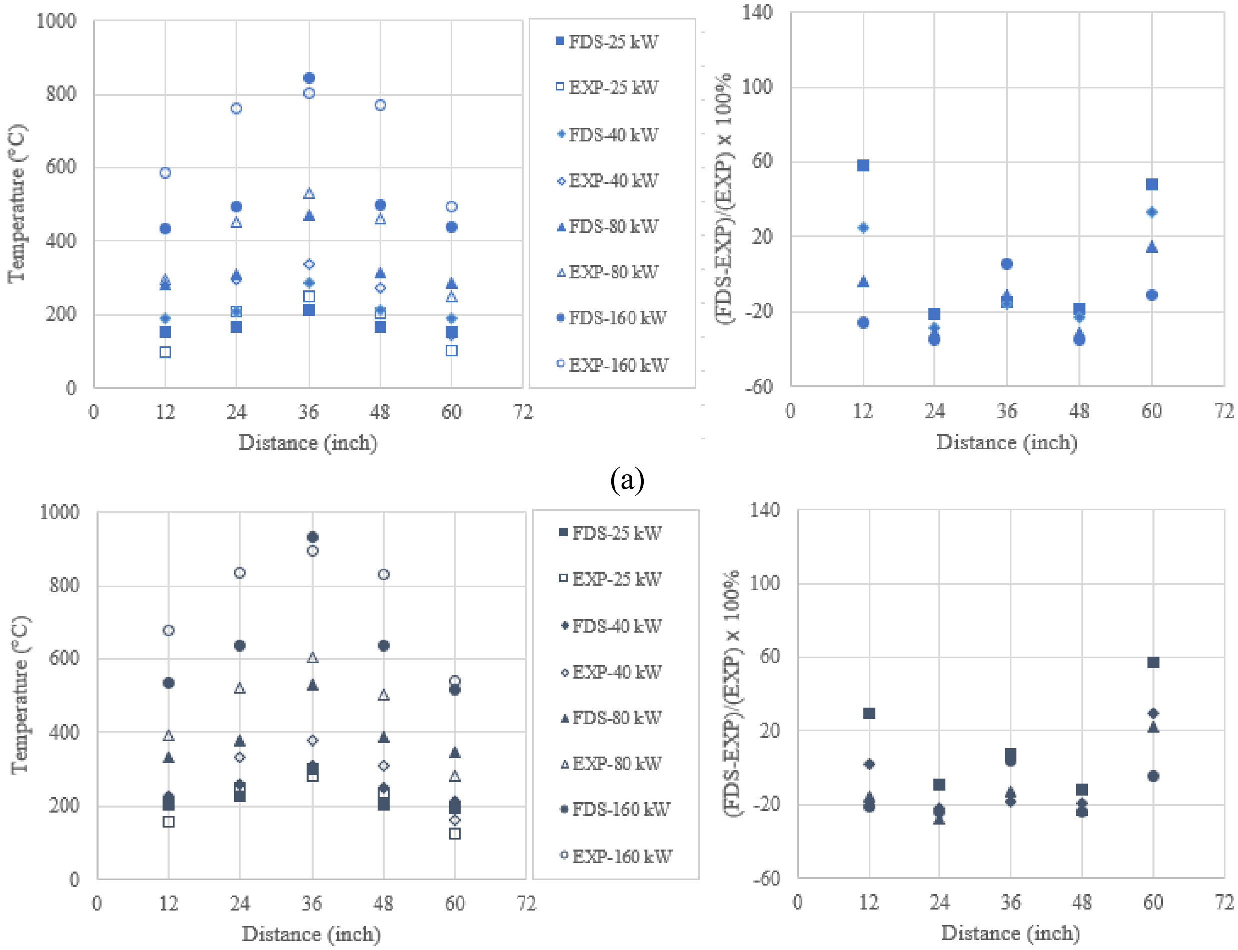

(a)

(b)

Figure 5.2 Comparison between experimental and numerical (a) average (b) maximum temperatures in BEAM3.

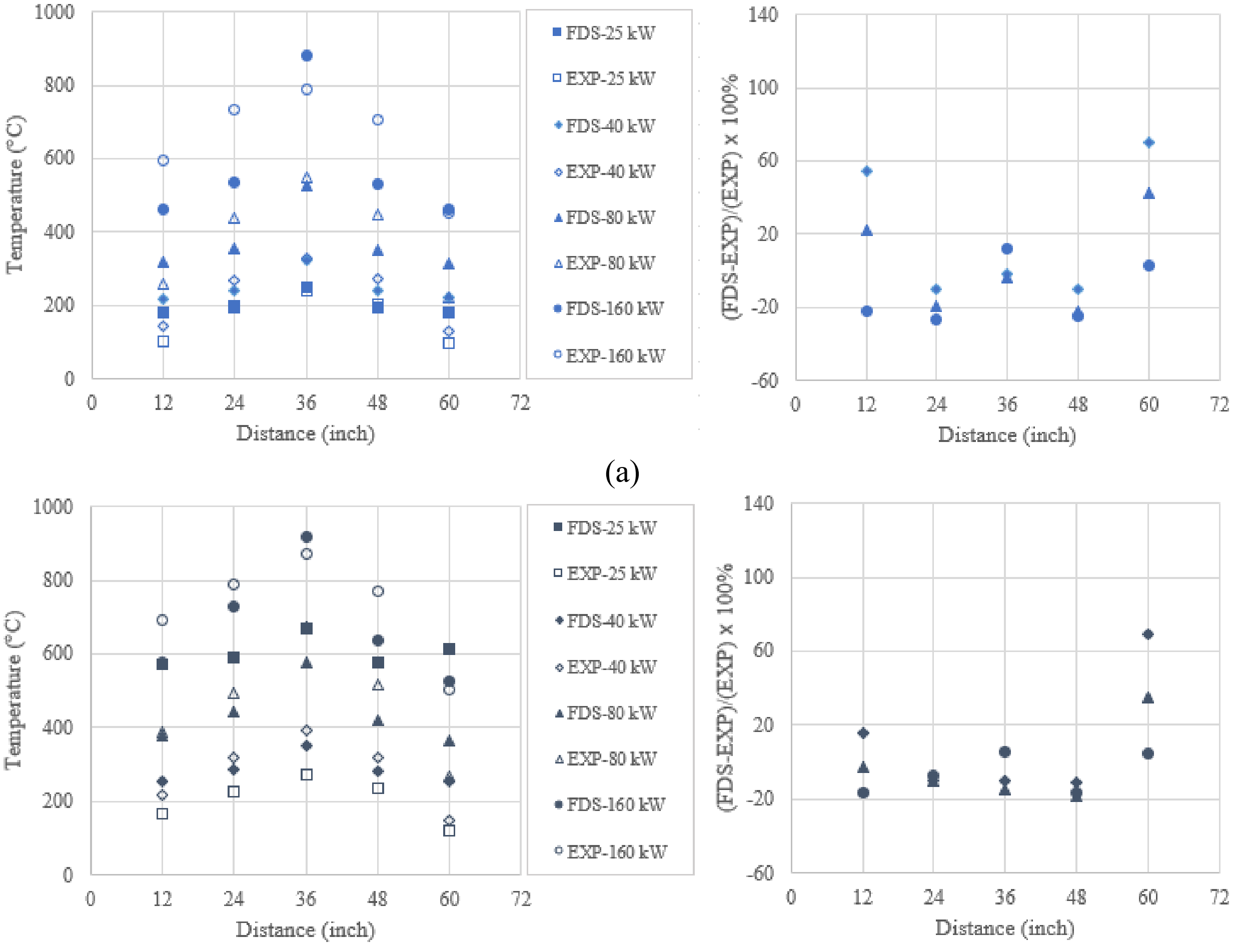

(a)

(b)

Figure 5.3 Comparison between experimental and numerical (a) average (b) maximum temperatures in BEAM2.

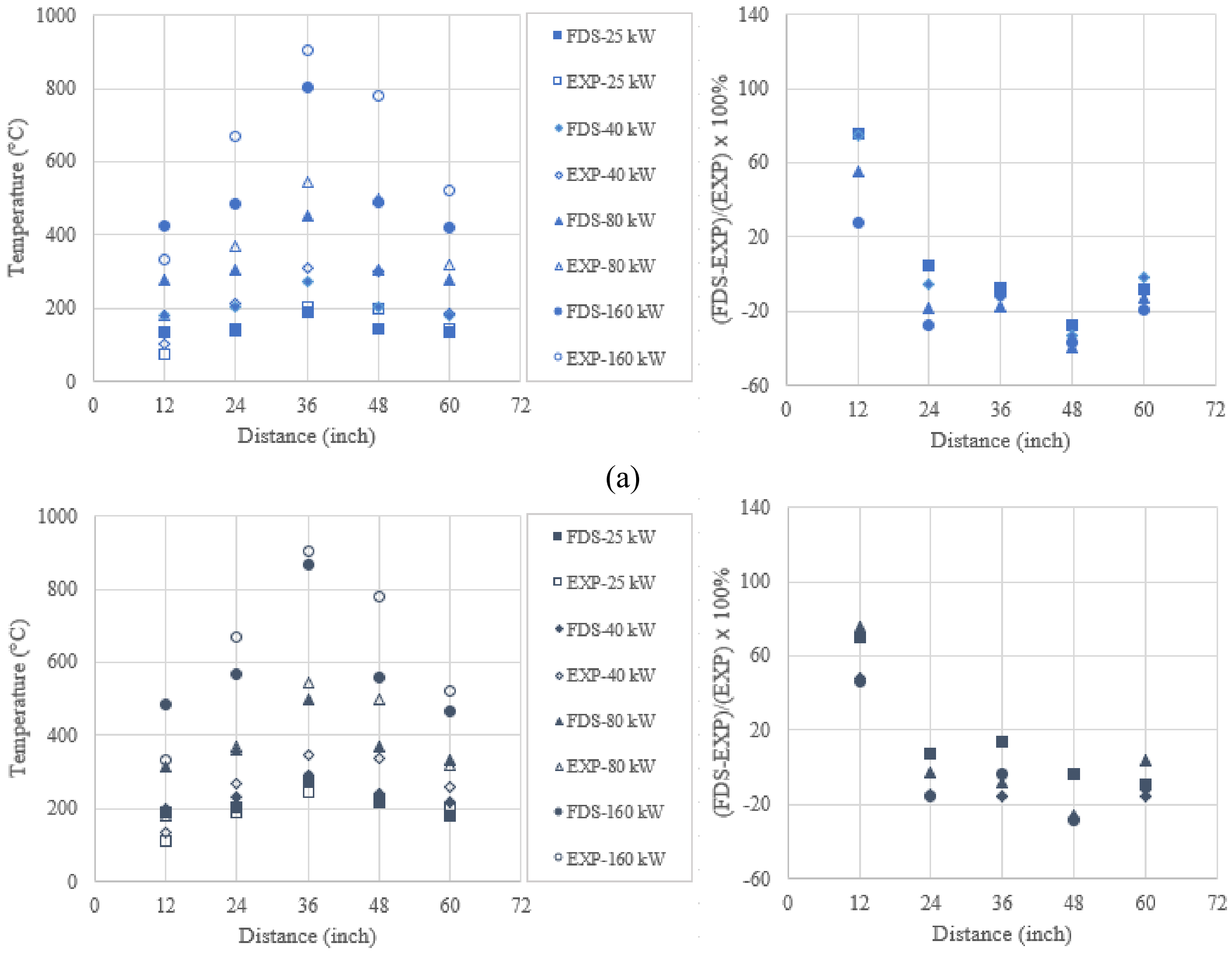

(a)

(b)

Figure 5.4 Comparison between experimental and numerical (a) average (b) maximum temperatures in BEAM1.

5.2 Uncertainty Analysis of FDS results

The differences between the numerical and experimental results can be attributed to measurement errors and inaccuracies in the FDS. The measurement errors mainly stem from incorrect measurements, such as when using HRR as input in the FDS as well as gas and inside beam temperatures. The model inaccuracies mainly stem from the geometrical differences, and physical assumptions of the numerical model (e.g., radiation parameters). The measurement uncertainty means the dispersion of the values of a measured variable.

5.2.1 Experimental Uncertainty

McGrattan et al. (2013c) described that the experimental uncertainty is calculated by k times the experimental relative standard deviation w_E of a measured variable (i.e., temperature in this study). k is assumed to be two for a 95% uncertainty interval.

The experimental relative standard deviation w_E can be calculated as follows:

$$w_E^2 = w_0^2 + \sum_i^n p_i^2 \, w_i^2 \tag{5.1}$$

where, w_0 is the relative standard deviation of the measured output and represents the device uncertainty for measuring temperatures; the factors p_i represent the power dependences of the individual input parameters; $w_i$is the relative standard deviation of the measured input and represents the device uncertainty for measuring input parameters in the numerical model; n is the number of variables affecting the experimental uncertainty. Since the HRR is the only input parameter in the numerical model, n is equal to 1. After this, equation (5.1) is applied to the present fire tests and the following equations are obtained.

$$w_E^2 = w_{temperatures}^2 + p_{temperature/HRR}^2 w_{HRR}^2 \tag{5.2}$$

$$w_{temperatures}^2 = w_{thermocouples}^2 + w_{datalogger}^2 \tag{5.3}$$

Since this specific tests were conducted at NIST, the suggested values for $p_{temperature/HRR}^2$, w_{HRR}, and $w_{thermocouples}$ are 2/3, 15%, and 0.75%, respectively, as named in McGrattan and Miles (2016) and McGrattana nd Toman (2011). If $w_{datalogger}$ is equal to 0.25% as the value used in the Valencia Bridge fires (Alos-Moya 2019), the experimental relative standard deviation, w_E is equal to 10.03%, and the final experimental uncertainty was 20.06% for a 95% uncertainty interval.

5.2.2 Model Uncertainty

Some assumptions must be considered to obtain the model uncertainty (Dréan et al. 2022, Dréan et al. 2018). 1) The uncertainty of the unbiased experimental measurements is normally distributed with a constant experimental relative standard deviation w_E; 2) The model uncertainty is normally distributed about the predicted uncertainty multiplied by a bias factor, δ. The bias factor δ indicates the numerical model is over- or under-predicting the experimental measurements; and 3) the numerical model relative standard deviation of temperature distribution is designated as w_M and is regarded as the scatter of the numerical output. The parameters w_M and δ for describing model uncertainty are calculated as follows based on the experimental uncertainty w_E, experimental measurements E_i, and corresponding model predictions M_i. The calculation of δ and w_i for the FDS uncertainty is required from the experimental temperatures and the FDS temperatures.

$$w_M^2 + w_E^2 = \frac{1}{n-1} \sum_{i=1}^{n} [\ln(M_i/E_i) - \ln(\overline{M}/E)]^2 \tag{5.4}$$

$$\delta = \exp\left[\ln(\overline{M}/E) + \frac{w_M^2}{2} - \frac{w_E^2}{2}\right] \tag{5.5}$$

where, $\ln(\overline{M}/E) = \frac{1}{n}\sum_{i=1}^{n} \ln(M_i/E_i)$

Figure 5.5 shows the scattering of average temperatures and maximum temperatures from the experimental and FDS for the four fire tests. The experimental temperatures were measured by the thermocouples in the five locations near the compartment wall. Figure 5.5(a) has 90 points, while Figure 5.5(b) has 85 points since the five maximum temperatures at the first constant HRR in BEAM2 were excluded as mentioned before. The bias factors (δ) are 1.014 and 0.975 for average and maximum temperatures, respectively. The dispersion of the FDS temperatures is attributed to the assumptions of the FDS model, and the uncertainties of the input parameters in the FDS (such as geometry, combustions, and windy conditions). Table 5.4 shows comparison of the parameters used for measuring uncertainty in different validation studies. Note that our study has the same experimental relative standard deviations as the Valencia Bridge fire tests (Alos-Moya et al. 2019). Although the numerical model relative standard deviations are higher than others, the bias factors are much lower than those in other studies.

Table 5.4 Maximum (Max) temperature (T)

Gas temperature	w_E	w_M	δ	Points
Concrete beam (Average)	0.100	0.306	1.014	90
Concrete beam (Max)	0.100	0.230	0.975	85
Valencia Bridge (Average)	0.100	0.237	1.291	70
Valencia Bridge (Max)	0.100	0.194	1.098	70
McGrattan et al. (2013c)	0.070	0.140	1.050	898

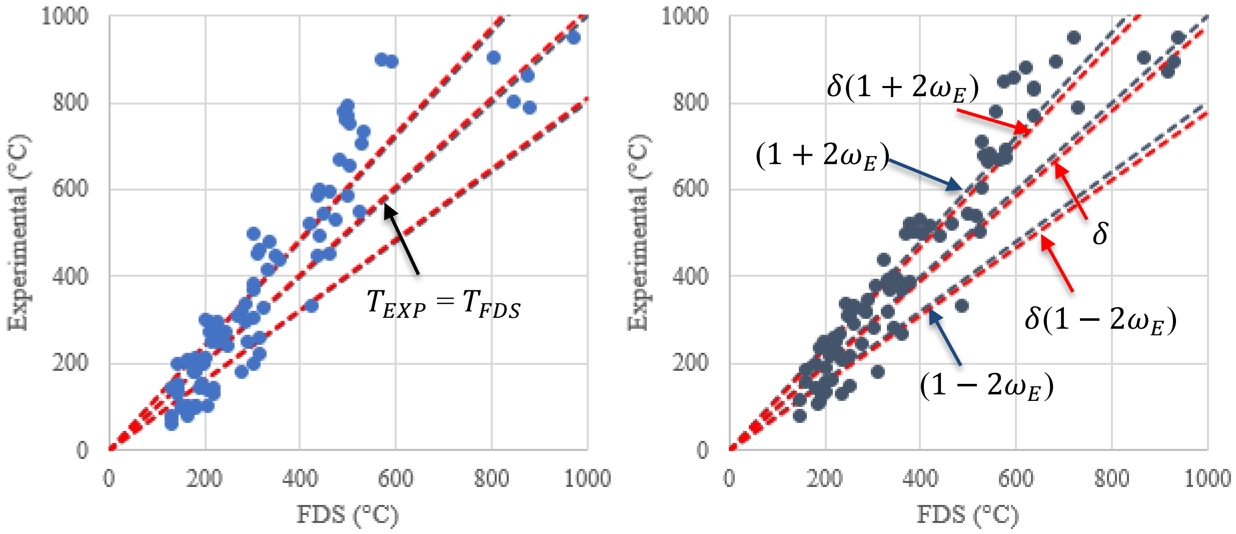

(a) (b)

Figure 5.5 Comparison between experimental and FDS (a) average temperatures (b) maximum temperatures.

Chapter 6 Parametric Studies

To obtain the best fit for the testing gas temperatures and more insights on the gas temperature and inside beam temperature development in the FDS, parametric studies are performed to investigate the different factors affecting the simulated temperatures. To simplify the simulation and comparison, the BEAM1 model is used as the reference case and the comparison is made between the five tested gas temperatures and simulated ones. Moreover, these parametric studies are beneficial for developing finite element model updating (i.e., an application in system identification) to obtain real-time updating to minimize the loss between the test gas temperatures and simulated ones. For example, the optimized wind effect as a function of time can be abstracted for future use after developing finite element model updating.

6.1 Mesh Size

Mesh size usually has significant effect on the computing time. A finer mesh requires longer time to converge. Mesh sensitivity analysis is needed to obtain an optimized mesh size to balance computing time and accuracy. The selected mesh size in this study refers to Chapter 3.1. If mesh size in BEAM1 reduces by two times, the computing time becomes about 33 hours, which leads the authors to increase mesh size. Two cases are considered in this parametric analysis.

If the number of cells for mesh increases from 4070 to 7995, the computing time is about 5.5 hours. The number of cells in the x, y, and z directions is 41, 13, and 15, with corresponding cell sizes of $0.0446 \times 0.0385 \times 0.0440$ m, respectively. Similarly, if the number of cells for mesh decreases from 4070 to 1296, the computing time is about 45 minutes. Figure 6.1 shows gas temperature comparison from the numerical models with different cell numbers. A finer mesh size can increase gas temperatures.

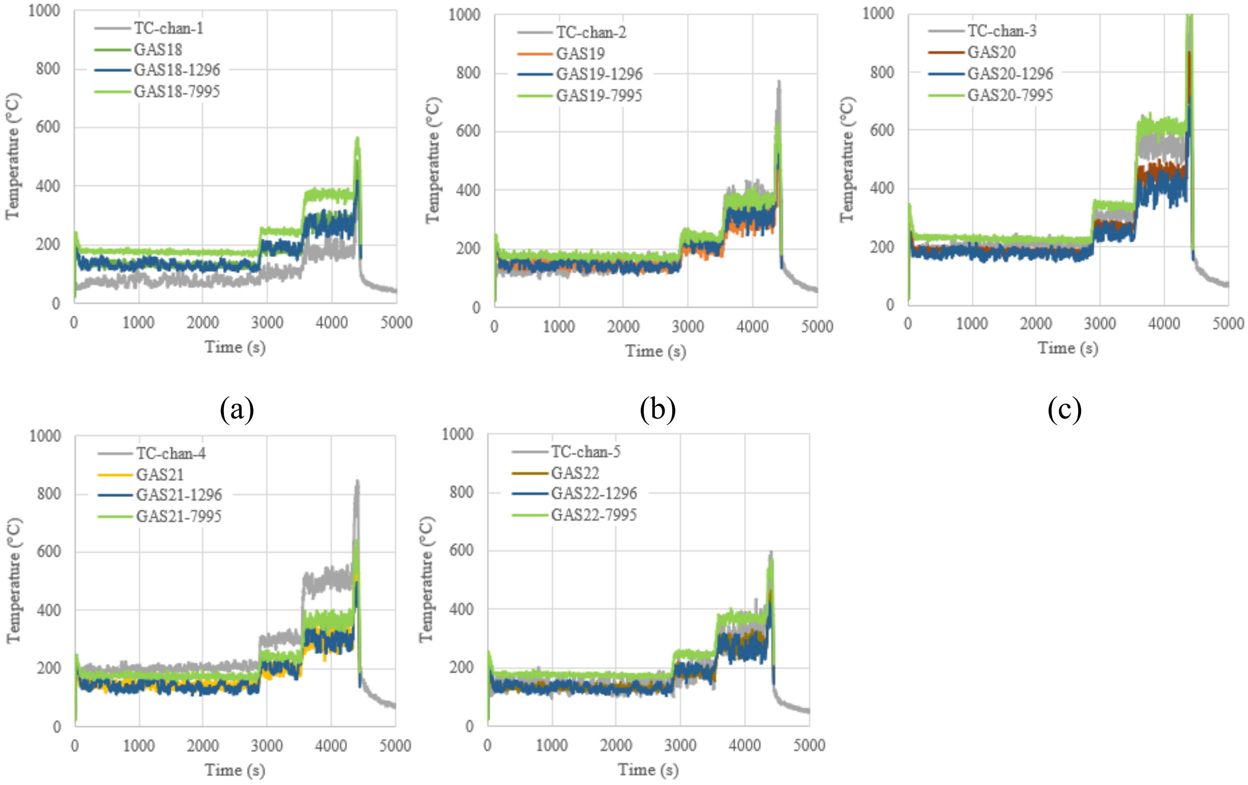

(a) (b) (c)

(d) (e)

Figure 6.1 Mesh size effect on gas temperatures of BEAM1.

6.2 Computational Zone

The computational domain can potentially affect computing accuracy and computing time. A theoretically calculated pool fire flame height provides a lower limit of the computational height estimated in a large-scale bridge (Timilsina et al. 2021). Although the channel fire is performed in this study, it is necessary to investigate the computational mesh zone effect on the gas temperatures. To obtain a fair comparison, the mesh size is consistent with BEAM1 when the computational zone increases two times as shown in Figure 6.2. It is found that the time needed to finish this computation is about 12 hours, while it is about 1.5 hours for BEAM1. However, no significant gas temperature difference is observed between them in addition to the gas temperature at the middle of the compartment wall (i.e., TC-chan-3) as shown in Figure 6.3.

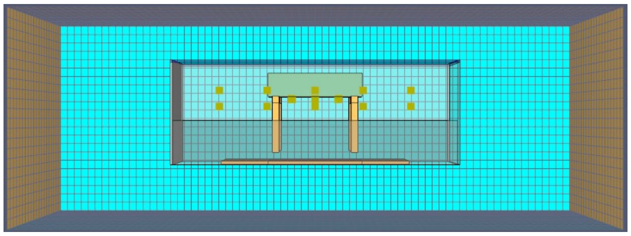

Figure 6.2 Increasing computational zone by two times.

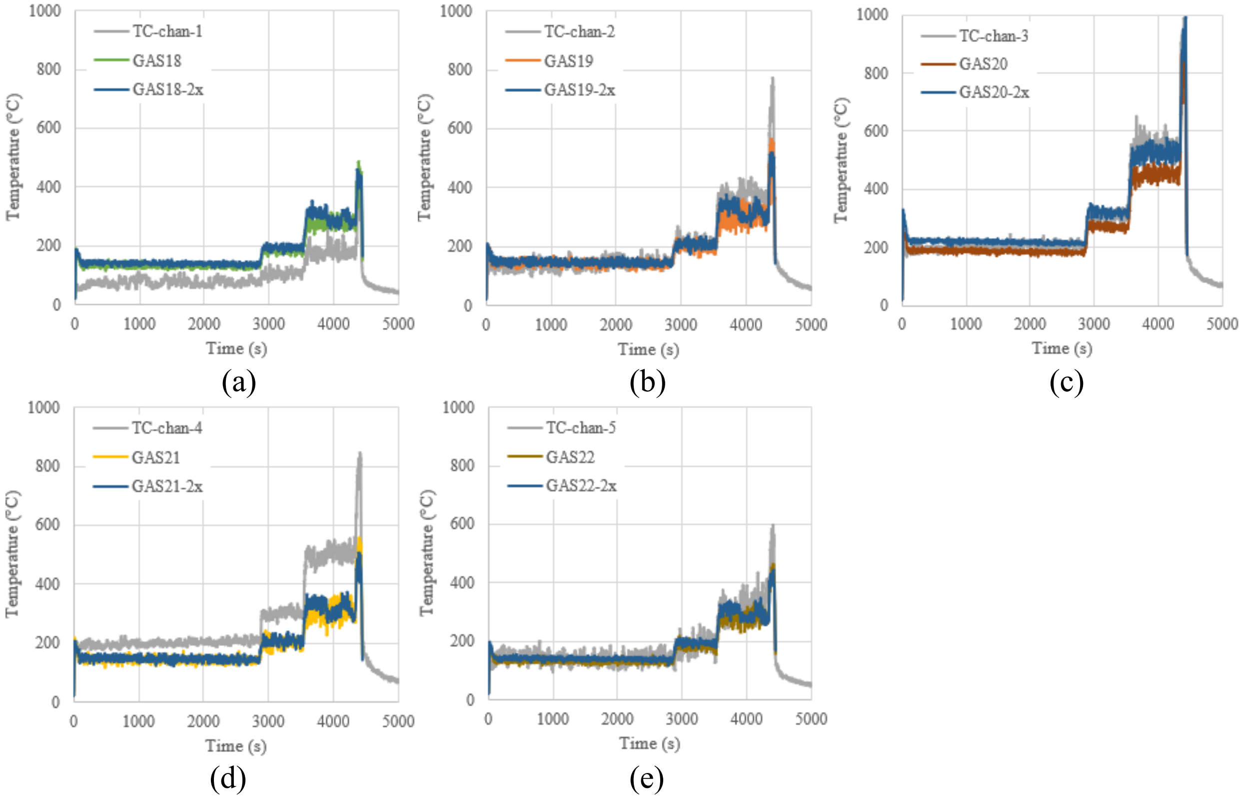

(a) (b) (c)

(d) (e)

Figure 6.3 Computing gas temperatures for two times computational zone.

6.3 Side Hole Area

Since the numerical model in the FDS has simplified geometry, the openings at the long side walls are considered as two holes in this study. However, these openings in the test were expanding the bottom area contacting with the air, which affected the air circulation from the fire source to the open boundary conditions. Also, the inclined obstruction in the FDS needs effort to be created. Figure 6.4 shows the numerical model with side hole area reduction by extending long side walls to approach the bottom. Figure 6.5 shows comparison of the numerical models with and without side hole area reduction. Obviously, the compartment gas temperatures increase as the hole area reduces due to hot gas exchange reduction.

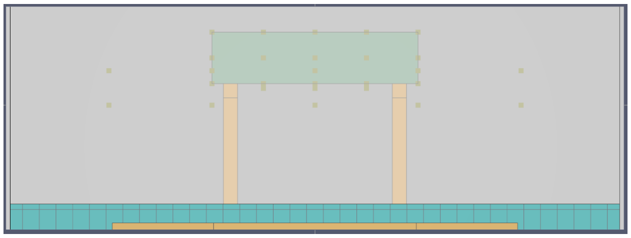

Figure 6.4 BEAM1 with the hole area reduction at both long sides.

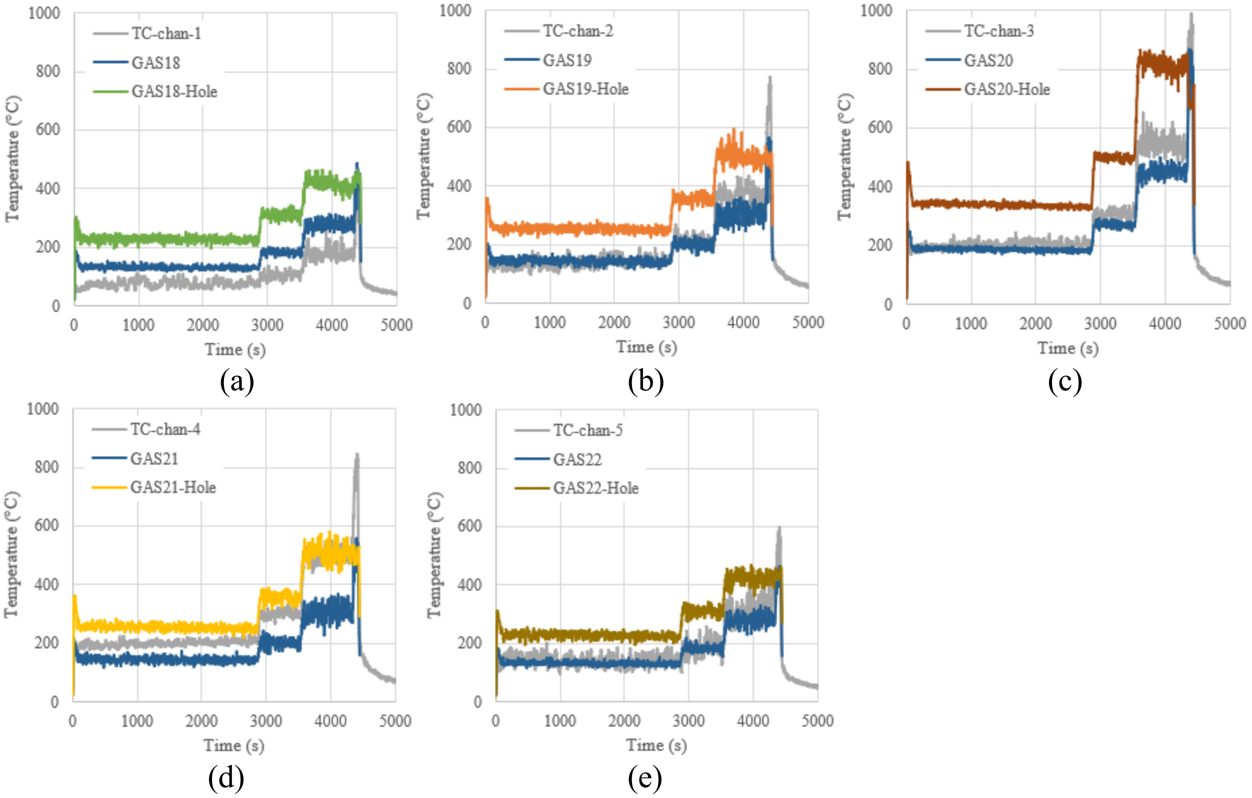

(a) (b) (c)

(d) (e)

Figure 6.5 Numerical and measured air compartment temperatures: BEAM1 with reduction inside hole areas.

6.4 Burner Surface Temperature

The temperature of the burner surface is needed for input in the FDS. However, this temperature shows a large deviation. A pool fire may remain 50-100 °C, equal to the boiling point of the liquid. Wood has an ignition temperature range between 200 °C and 700 °C. Natural gas fueled porous burner has temperature range from 530-750 °C. Therefore, a burner surface temperature of 530 °C was considered in BEAM1 to investigate its effect as shown in Figure 6.6. It is found that burner surface temperature does not affect the gas temperatures compared to the burner surface temperature of 300 °C.

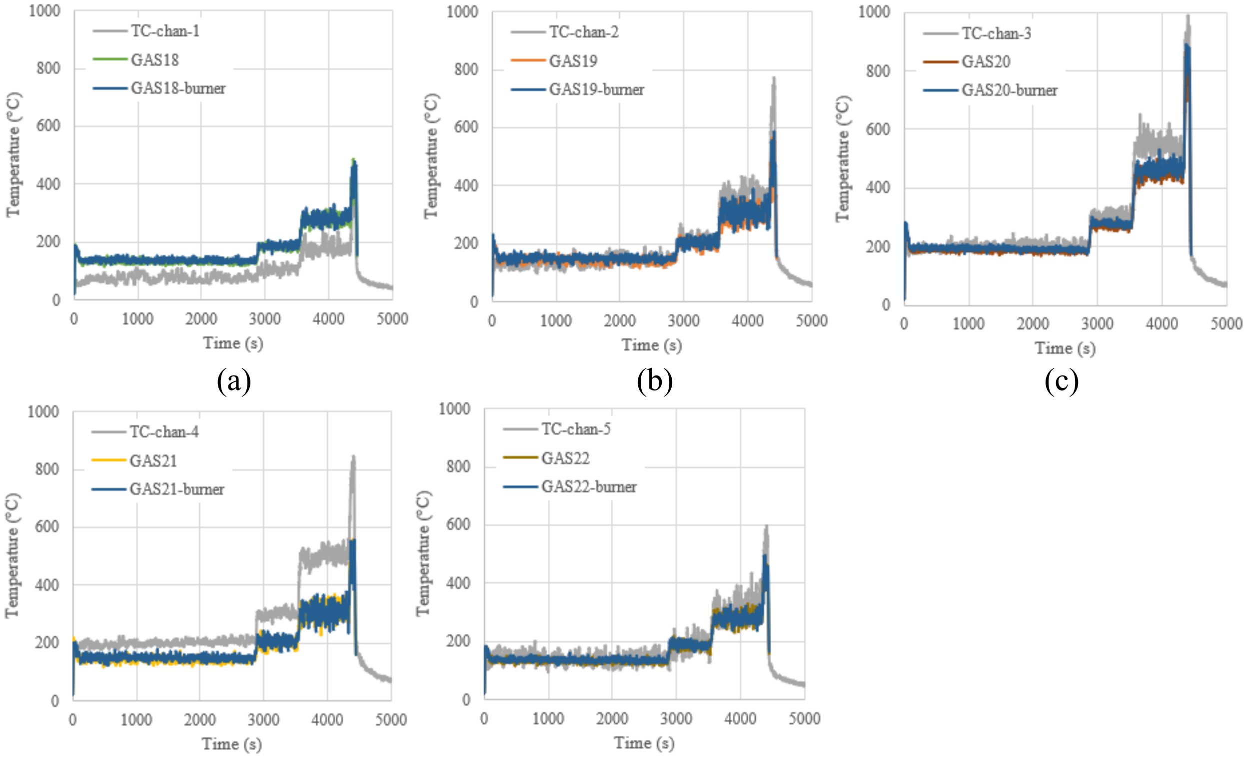

(a) (b) (c)

(d) (e)

Figure 6.6 Numerical and measured air compartment temperature: BEAM1 with different burner surface temperatures.

6.5 Layer Material Thickness and Properties

FDS can perform a transient, one-dimensional calculation of heat transfer into solid obstruction surfaces (i.e., concrete beam in this study), which achieves an appropriate estimate and fast computation of real heat conduction. When performing a specific modeling, it is importation to select suitable parameters and match them to a practical test case to obtain layer temperatures inside solid obstruction. These discussions include material input, surface input, and obstruction input (i.e., surface combination). First, the basic parameters in BEAM1 are introduced in detail. The thermal properties include a density of 2280 kg/m^3, specific heat of 1.04 kJ/(kg.K), conductivity of 1.8 W/(m.K), emissivity of 0.9, and absorption coefficient of 5.0×10^4 1/m. The material emissivity is to calculate radiative heat flux from the surface and the absorption coefficient describes the energy deposits through the radiation penetration. The default absorption coefficient stores the radiation energy at the boundary surface without penetration. In the material definition, the solid pyrolysis is not included. For the concrete surface, the material layer thickness is 0.152 m, and the material composition is 1.0CONCRETE. The initial internal temperature equals the ambient temperature. The exposed option is selected for the backing side boundary condition first.

A specific explanation of three boundary conditions of the back side of the surface is shown in Figure 6.7. The insulated option means there is no heat lost from the back side of the material. The void (air gap) option means the back surface is open to ambient temperature and radiative and convective heat fluxes removes heat. The exposed option can couple the back of surface 1 to the front of surface 2 or the front of surface 1 to the back of surface 2, which achieves heat conduction through obstruction. Heating the front of surface 1 increases the temperature of the front of surface 2, and vice versa. However, the exposed option has constraints on the geometry of the obstruction. The obstruction is less than one cell thick or equal to one cell thick with a non-zero volume of computational domain on the other side of the obstruction. If the obstruction is on domain boundary (where the front of surface 2 is not exposed to gas) or if the obstruction is more than one cell thick, the boundary is changed to void and exposed to an air gap at ambient temperature. Only the Temperature Calculated option is selected for the front side boundary condition.

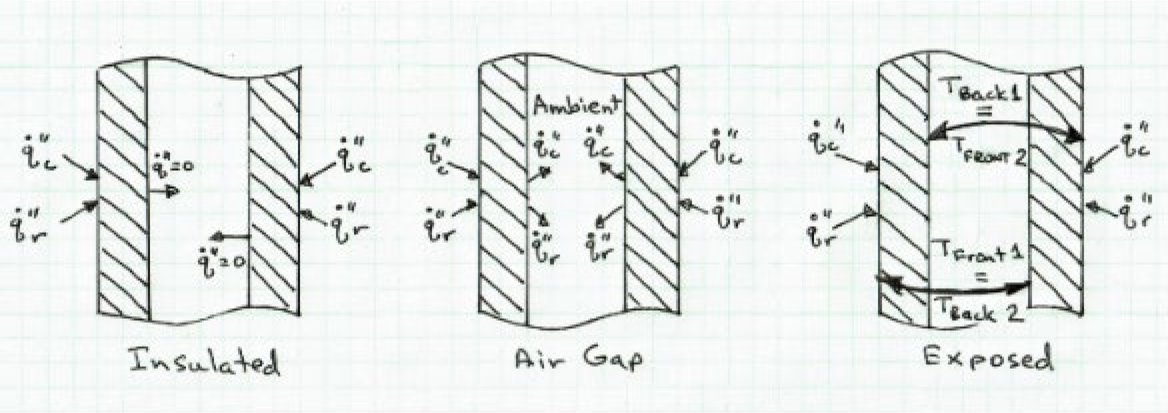

Figure 6.7 Illustration of the boundary conditions on the back side of a surface (where $\dot{q}''_c$ is convective heat flux, $\dot{q}''_r$ is radiation heat flux, and $\dot{q}''$ is heat flux).

Different solid-phase devices are added to the concrete beams to obtain inside temperatures. The positions of these devices are consistent with the inside thermocouples as shown in Figure 6.8(a) and the simulated temperatures are compared with measured ones. Since these solid-phase devices must be associated with a heat-conducting surface, different internal wall temperature devices need to be defined with a normal direction at different surfaces of the concrete beam. This conclusion is confirmed from the comparison between Figure 6.8(b) and (c). Although Figure 6.8(b) has all six surfaces assigned a concrete surface with a predefined layer thickness of 0.152 m, only internal wall temperature devices with respect to the bottom surface are defined. Therefore, Figure 6.8(c) with only the bottom surface assigned a concrete surface shows the same temperature as Figure 6.8(b). For each concrete beam surface, corresponding internal wall temperature devices should be defined and the modeling temperatures at the same location can superpose for temperature comparison. Before comparing them, the modeling temperatures with an air gap boundary condition used for the back side of the material are presented in Figure 6.8(d). Again, it shows the same temperatures as Figure 6.8(c) since the exposed boundary condition in this study is not satisfied and invalid due to the larger thickness of the concrete beam.

Figure 6.9 shows the temperature magnitudes at the four locations collected from different concrete surfaces (i.e., two sides and top surface) in BEAM1. We can see the temperature contributions from other concrete surfaces rather than bottom surface are small. Figure 6.10 shows the superposition temperatures at the four locations in BEAM1 and the FDS temperatures are compared with the test temperatures. It is found that the measured temperature at the TC4 matches well with the FDS one. Similarly, Figure 6.11 shows superposition FDS temperatures in BEAM2, which are compared with the thermocouples. Figure 6.11(b) excludes the TC4 due to the malfunction. However, it is noticed that the environmental temperature of 27.4 ℃ shows a better prediction than 58.8 ℃, especially in the initial stage. Although the compartment gas temperature increases to 58.8 ℃ due to the response time delay as discussed in Chapter 4, the temperatures in the concrete beam are still not high. Moreover, Figure 6.12 shows a comparison between FDS and measured temperatures in BEAM3 and BEAM4. Overall, it is found that the FDS shows a good prediction for the TC4 and gives upper and lower limits for the experimental temperatures.

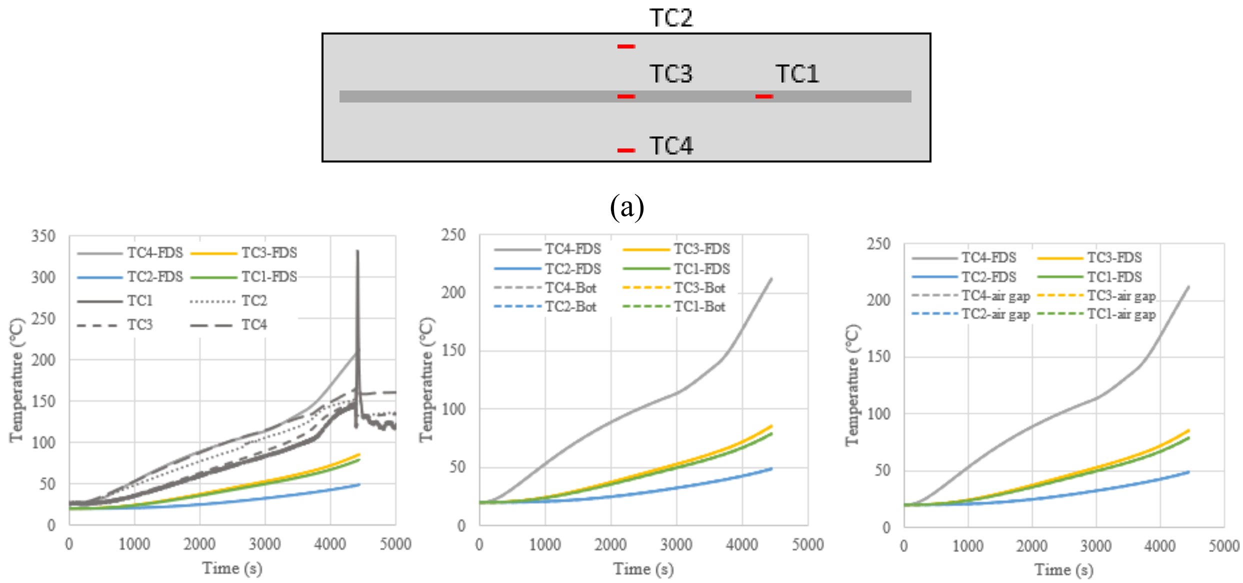

(a)

(b) (c) (d)

Figure 6.8 (a) Thermocouples arranged in concrete beams; (b) comparison between measured and FDS temperatures (with six concrete surfaces, but the temperature devices corresponding to bottom surface only); (c) one bottom concrete surface and its corresponding temperature devices; (d) effect of exposed and air gap boundary condition for the back side of material in BEAM1.

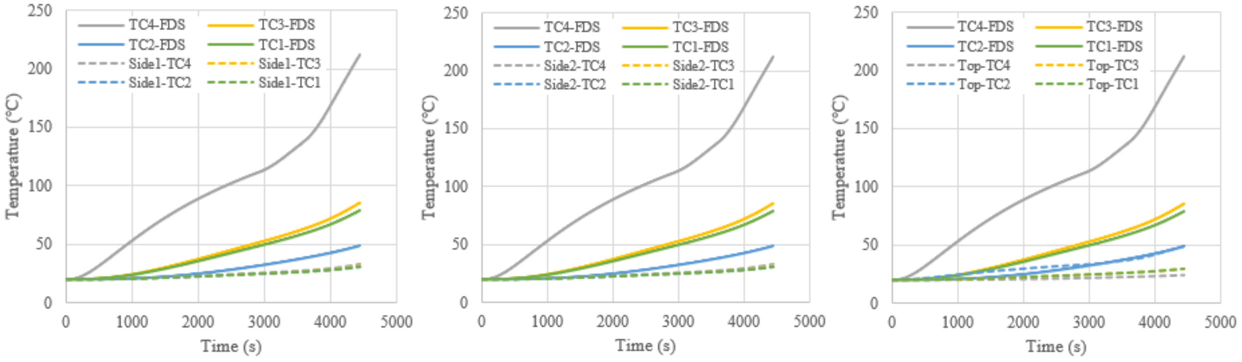

(a) (b) (c)

Figure 6.9 Temperatures at four thermocouple locations conducted from (a) (b) side surfaces (c) top surface, Change inside layer surface and corresponding devices.

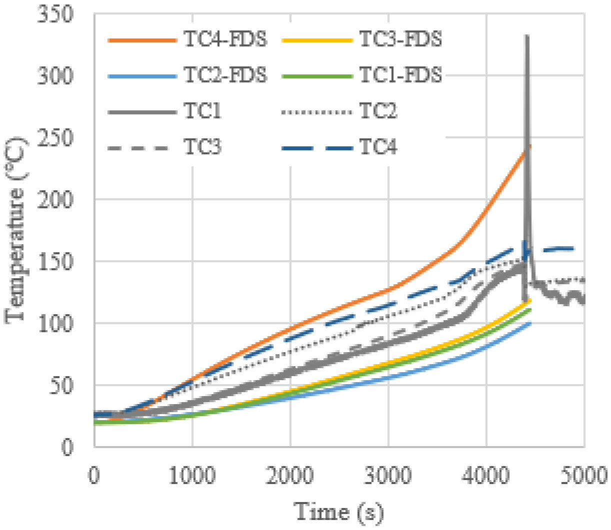

Figure 6.10 Superposition temperatures from different concrete surfaces compared with thermocouple temperatures in BEAM1.

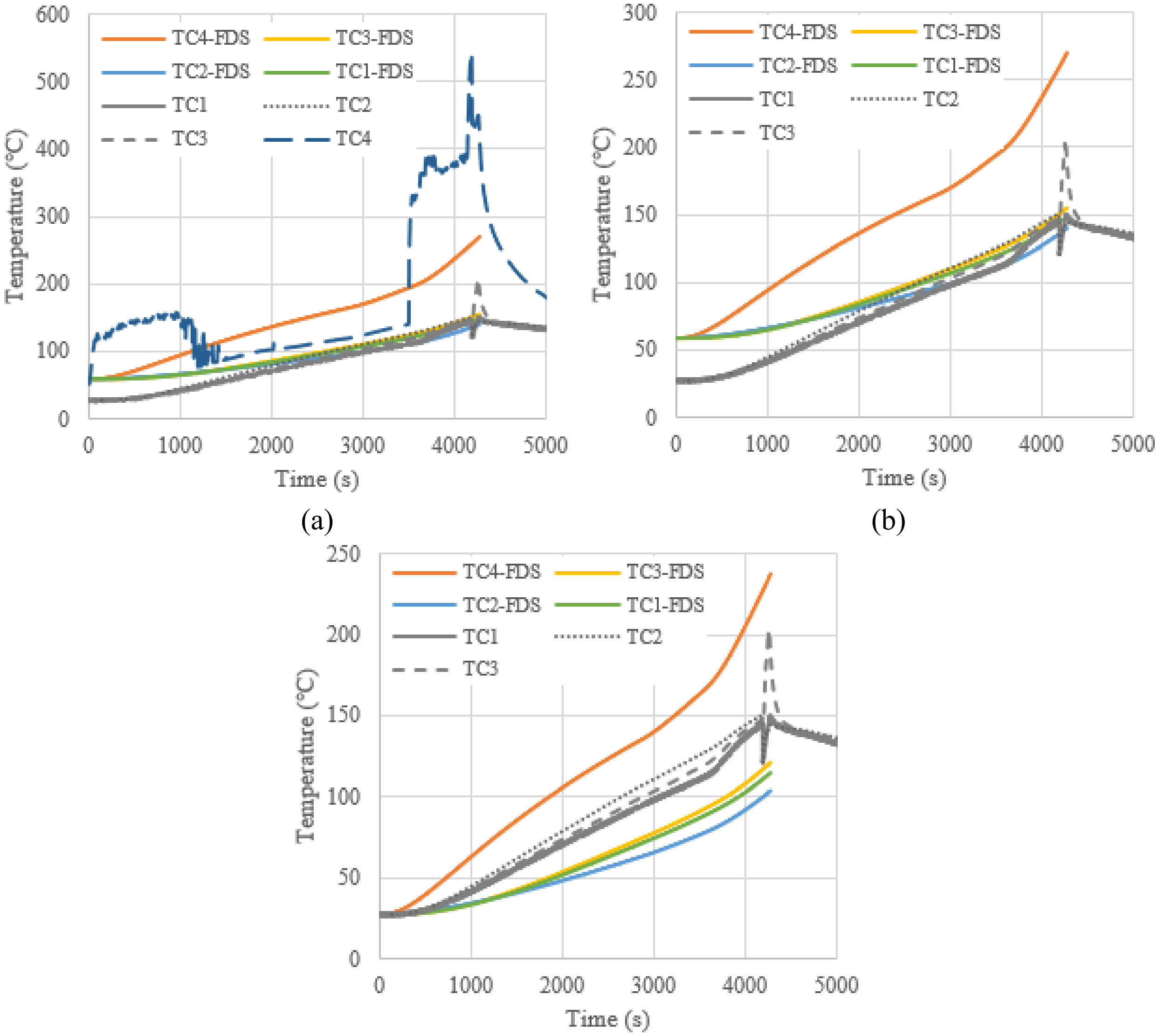

(a)

(b)

(c)

Figure 6.11 (a) Comparison between FDS and test temperatures in BEAM2 (b) excluding TC4 (c) considering environmental temperature parameter of 27.4 °C instead of 58.8 °C in (a) and (b).

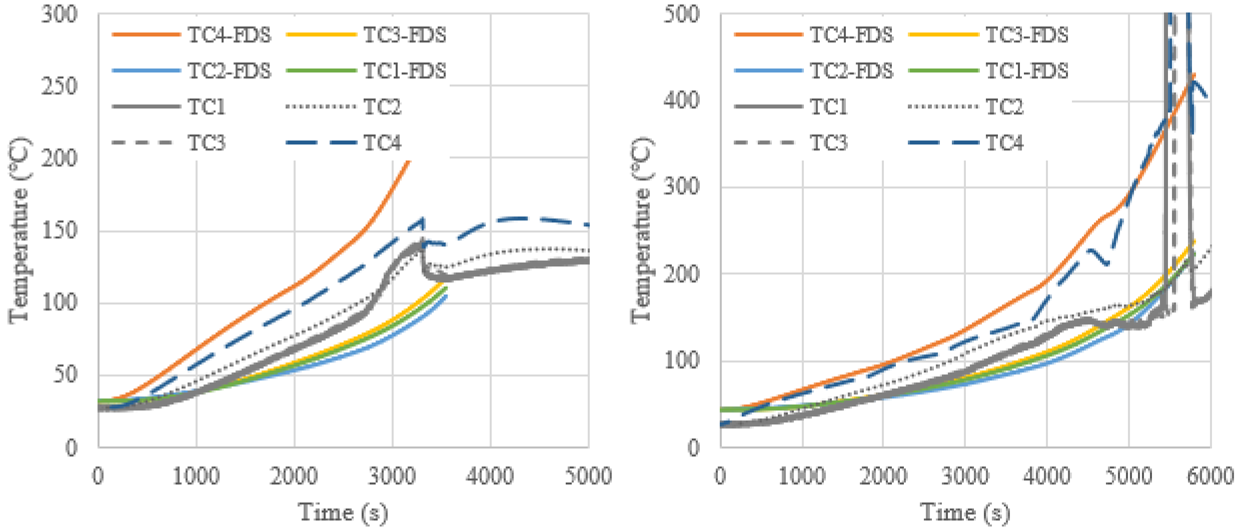

(a) (b)

Figure 6.12 Comparison between FDS and test temperatures in (a) BEAM3 and (b) BEAM4.

6.5.1 Surface Input

Since the layer thickness and number of layers may affect one-dimensional heat conduction, the inside temperature sensitivity could fluctuate when changing these parameters. Figure 6.13 shows the effect of the layer thickness change from 0.152 m to 0.05 m (approximate mesh size) on the inside temperatures. Note that this figure only shows the device-measured temperatures collected from the bottom of the concrete beam (BEAM1). It is found that layer thickness change in the obstruction increases three other temperatures in addition to the TC3 due to convection and radiation but does not affect FDS calculated gas temperatures. Figure 6.14 shows the effect of the number of layers of the concrete surfaces on the temperatures. The concrete beam was divided into different layers with equal thickness to see its effect on the heat conduction. Four layers and ten layers are assigned to the top, bottom, and two long side concrete surfaces of BEAM1, no changes in two end caps. It is found that their effect on the temperatures can be neglected as shown in Figure 6.14 since the air void boundary condition for the back side of the material is effective.

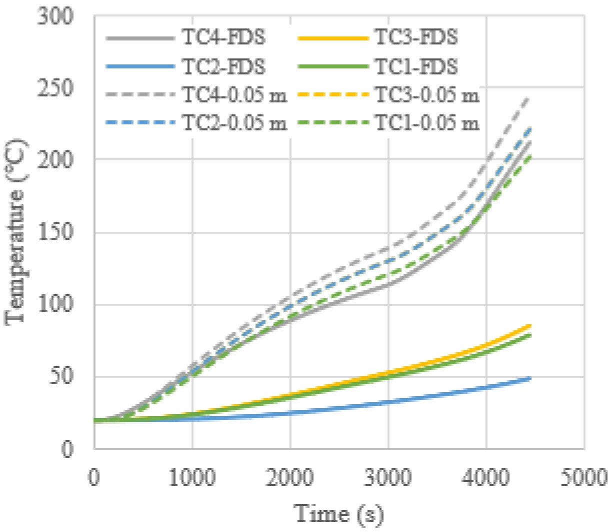

Figure 6.13 Effect of layer thickness change on the temperatures.

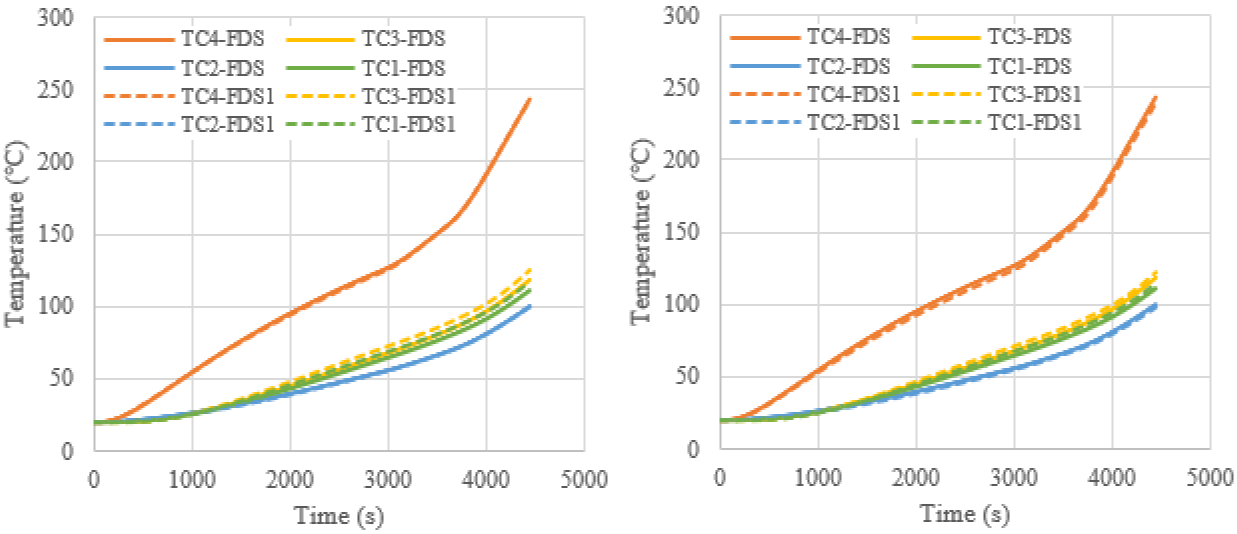

(a) (b)

Figure 6.14 Effect of number of layers on the temperatures (a) four layers (b) ten layers.

6.5.2 Material Input

Since the thermal properties can directly influence the one-way heat conduction, the effect of different material input on the temperatures is desirable. The main thermal properties include heat conductivity and specific heat, and both are temperature dependent. Based on EN 1994-1-2 General rules-structural fire design, the specific heat may be considered to be independent of the concrete temperature for simple calculation models, and the value of 1.0 kJ/(kg·K) can be taken, which is approximately equal to the value used for BEAM1 in the FDS. Otherwise, the specific heat (c_c) of normal weight dry, siliceous or calcareous concrete may be determined from following equations:

$$c_c = 900 \text{ for } 20\ ℃ \leq T \leq 100\ ℃ \tag{6.1}$$

$$c_c = 900 + (T\text{-}100) \text{ for } 100\ ℃ \leq T \leq 200\ ℃ \tag{6.2}$$

$$c_c = 1000 + (T\text{-}200)/2 \text{ for } 200\ ℃ \leq T \leq 400\ ℃ \tag{6.3}$$

$$c_c = 1100 \text{ for } 400\ °\mathrm{C} \leq T \leq 1200\ ℃ \tag{6.4}$$

where T is the concrete temperature (°C).

Moreover, an approximate function to describe the variation of c_c with the temperature can be expressed by:

$$c_c\ (T) = 890 + 56.2\ (T/100)\text{-}3.4(T/100)^2 \tag{6.5}$$

Figure 6.15 shows the effect of specific heat calculated by stepwise equations, approximate function, and constant value on the temperatures. Since the value used for BEAM1 in the FDS was 1.04 kJ/(kg·K), which is close to the code values, no significant effect can be seen from Figure 15(a) and (b). However, a specific value of 1.7 kJ/(kg·K) induces a significant reduction in temperatures as shown in Figure 6.15(c).

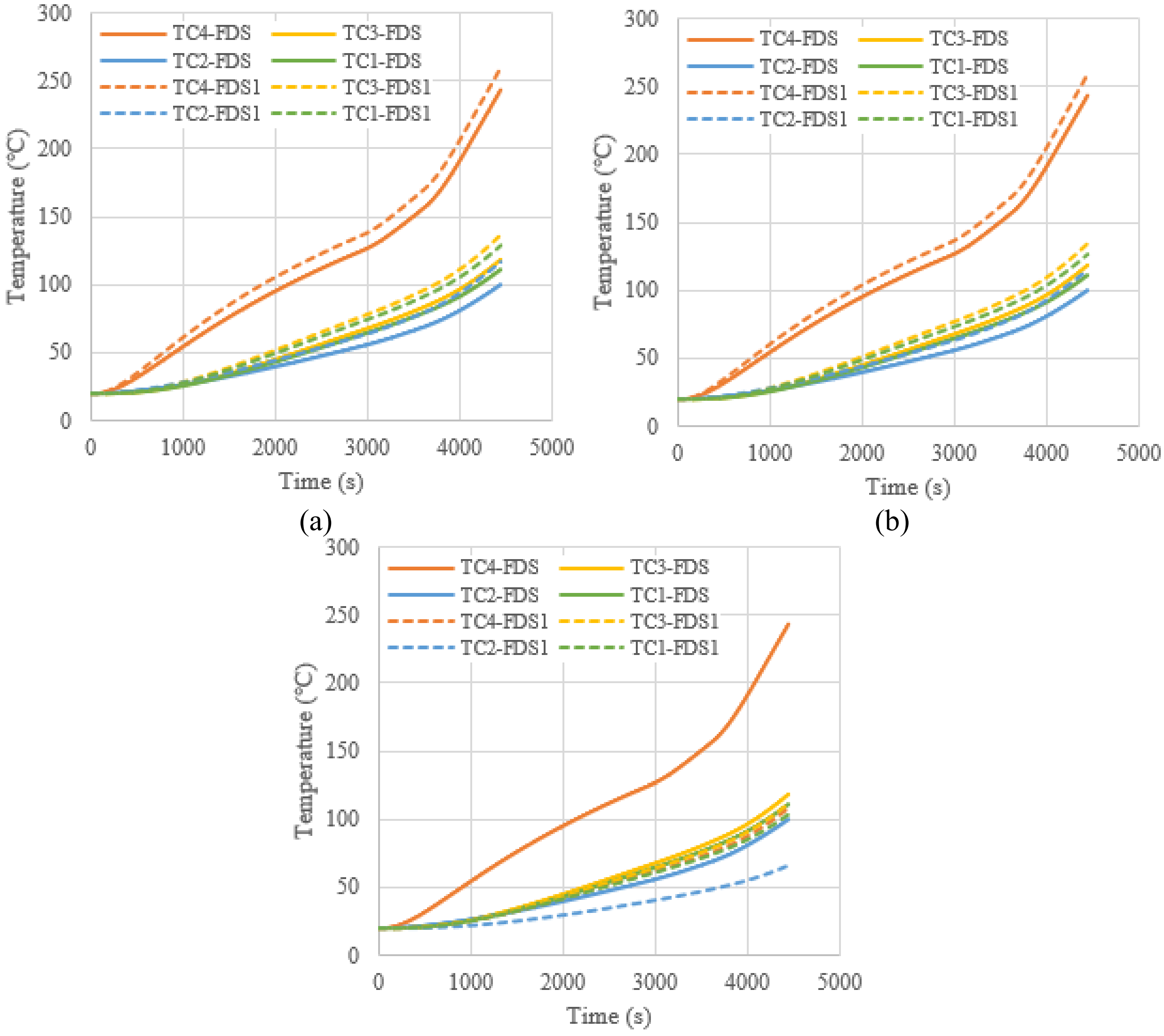

(a) (b)

(c)

Figure 6.15 Effect of specific heat on the temperatures (a) using stepwise specific heat equations (b) using an approximate specific heat function (c) using a specific heat value of 1.7 kJ/(kg·K) reported in Bao et al. (2017).

Similarly, thermal conductivity may be independent of the concrete temperature, and the value of 1.6 W/mK can be taken in the code, which is approximately equal to 1.8 W/mK used in the FDS. Moreover, the thermal conductivity λ_c of normal concrete can be determined between the lower and upper limits given in the following equations. From Figure 6.16, the small effect of the thermal conductivity calculated by the upper and lower limit functions on the temperatures can be observed.

The upper limit:

$$\lambda_c = 2 - 0.2451(T/100)+0.0107(T/100)^2 \text{ for } 20\ ℃ \leq T \leq 1200\ ℃ \tag{6.6}$$

The lower limit:

$$\lambda_c = 1.36 - 0.136(T/100)+0.0057(T/100)^2 \text{ for } 20\ ℃ \leq T \leq 1200\ ℃ \tag{6.7}$$

where T is the concrete temperature (℃).

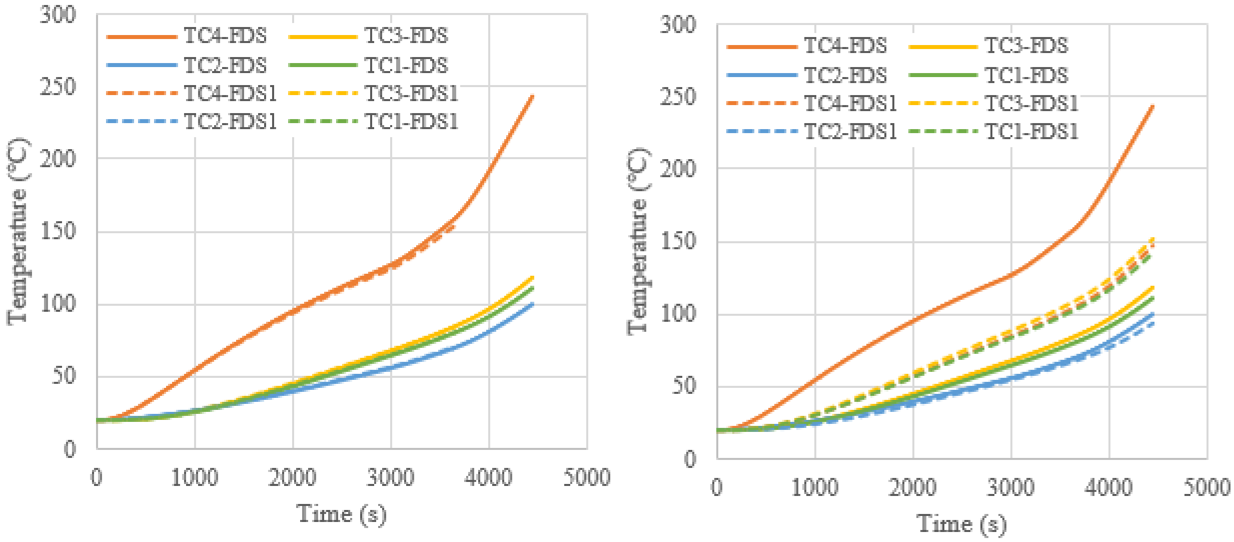

(a) (b)

Figure 6.16 Effect of thermal conductivity on the temperatures (a) using an upper limit function (b) using a lower limit function.

6.5.3 Other Relevant Factors

In the previous sections, the temperatures are directly defined and measured in the FDS. Therefore, the thermocouples are added to record temperatures for comparison at the same locations. The basic parameters for thermocouples in the FDS are as follows: bead diameter of

1.0 mm; emissivity of 0.85; bead density of 8908.0 kg/m^3; bead specific heat of 0.44 kJ/(kg.K). and these parameters are default values since they are unknown for the thermocouples in the test where it was claimed that each test beam was instrumented with four, glass sheath, K-type, bare-bead thermocouples. From Figure 6.17(a), in the air environment, they can measure the same temperature change, while the thermocouple devices defined in the obstruction in the FDS do not show temperature increase and keep constant initial temperature. Since the gas-phase device for gas temperature in the FDS at the solid surface does not function, the solid-phase device for gas temperature has a temperature as shown in Solid43 and compared with the wall temperature at the same location to see their difference in Figure 6.17(b). Since the adiabatic surface temperature can be an input for structural fire behavior prediction, it is meaningful to obtain this temperature. Dring testing, it is observed whether the adiabatic surface temperatures are the same when the adiabatic surface and the heat-conducting surface (i.e., layered surface) are applied. The bottom layered surface of the concrete beam is replaced by the adiabatic surface. It is found there is not much of a difference as shown in Figure 6.17(c). However, once the adiabatic surface is applied, the inside wall temperature devices corresponding to the bottom surface become invalid.

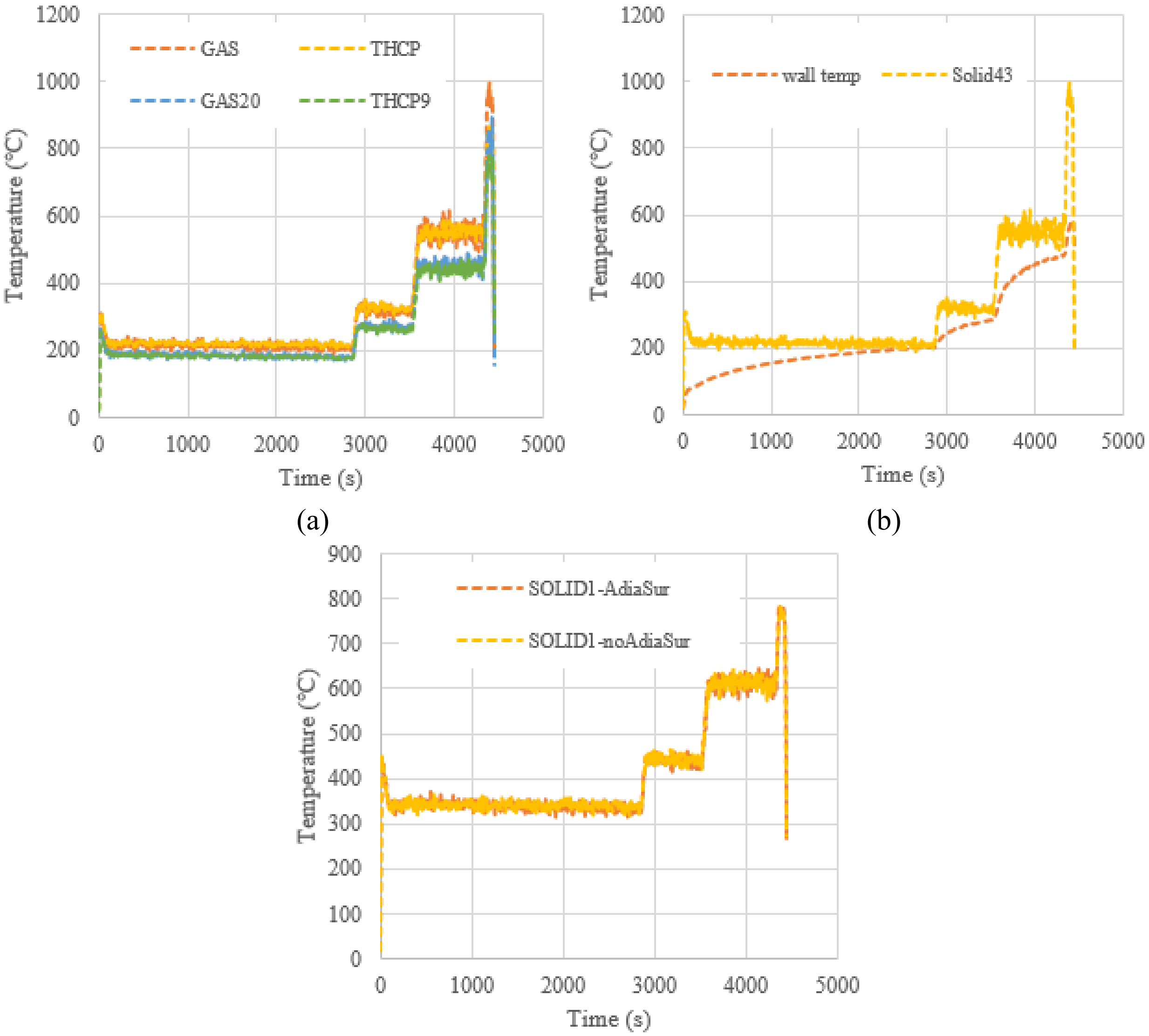

(a) (b)

(c)

Figure 6.17 (a) thermocouple device effect (b) solid- and gas-phase device effect for gas temperature (c) adiabatic surface effect.

6.6 Wind Effect

The concrete beams were tested in a national fire research laboratory and a practical wind condition was not monitored during the test. However, the wind does influence the flame movement from the experimental observations. Therefore, to reasonably consider wind effect in the FDS may be of interest to the readers. Three different ways can be defined to specify wind in the FDS. The first method is to model the wind and corresponding temperature profile using Monin-Obukhov similarity theory. The second is to specify a uniform horizontal forcing function and allow the wind field to develop naturally; this method has proven more useful in wind tunnel applications than for natural winds. The third is to create a wind wall, which indicates an entire computational domain side being a giant fan to blow air laterally; this method is not preferred to create winds. Therefore, the first method is applied in this study, i.e., Monin-Obukhov Similarity is used to simulate an atmospheric boundary layer in the FDS. The wind speed profile, u, and potential temperature, θ, vary with height, z, as follows:

$$u(z) = \frac{u_*}{\kappa} [\ln (\frac{z}{z_0}) - \psi_m(\frac{z}{L})] \tag{6.8}$$

$$\theta(z) = \theta_0 + \frac{\theta_*}{\kappa} [\ln (\frac{z}{z_0}) - \psi_h(\frac{z}{L})] \tag{6.9}$$

where u_* is the friction velocity, κ is the Von Kármán constant equal to 0.41, z_0 is the aerodynamic roughness length, θ_* is the scaling potential temperature, θ_0 is the ground level potential temperature (20 °C), L is the Obukhov length (describing the thermal stability of the atmosphere), and the similarity functions are as follows:

$$\psi_m(\frac{z}{L}) = \begin{cases} -5\frac{z}{L}, \ L \geq 0 \\ 2\ln\left[\frac{1+\zeta}{2}\right] + \ln\left[\frac{1+\zeta^2}{2}\right] - 2tan^{-1}(\zeta) + \frac{\pi}{2}, \ L < 0 \end{cases} \tag{6.10}$$

$$\psi_h(\frac{z}{L}) = \begin{cases} -5\frac{z}{L}, \ L \geq 0 \\ 2\ln\left[\frac{1+\zeta^2}{2}\right], \ L < 0 \end{cases} \tag{6.11}$$

$$\zeta = (1 - \frac{16z}{L})^{1/4} \tag{6.12}$$

If these various parameters are not reported or known, they can be approximately calculated from the basic meteorological conditions. The friction velocity can be calculated from a single measured mean wind velocity as follows:

$$u_* = \frac{\kappa u_{ref}}{\ln\left(z_{ref}/z_0\right)} \tag{6.13}$$

The suggested values of the aerodynamic roughness length, z_0, and Obukhov length, L can be chosen from Table 18.1 and Table 18.2 in the Fire Dynamic Simulator-User's Guide (Sixth Edition). Similarly, the scaling potential temperature can be calculated as follows:

$$\theta_* = \frac{{u_*}^2 \theta_0}{g \kappa L} \tag{6.14}$$

Figure 6.18 shows the sample vertical wind and temperature profiles. The parameters used to calculate these profiles are presented in the image below. The ground level height was set at zero. Then, its corresponding numerical results are shown in Figure 6.19(a) where the wind effect can be clearly demonstrated. Figure 6.19(b) shows the northerly wind blowing at 0.2 m/s, taken at a height 2 m off the ground, and only the initial wind speed at the reference height is different from the case in Figure 6.19(a). Therefore, it is demonstrated that the wind speed has an effect. Figure 6.19(c) shows the influence of the ground level height, which equals -1.143 m in the model, and other parameters are the same as the case in Figure 6.19(b). The ground level height affects the wind profile.

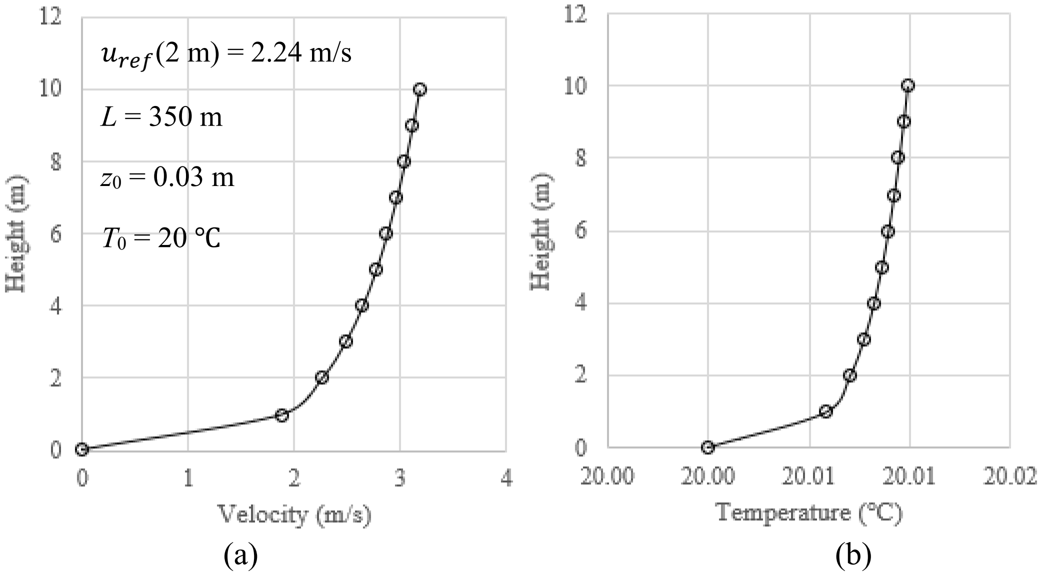

Figure 6.18 Sample vertical wind (a) and temperature (b) profiles

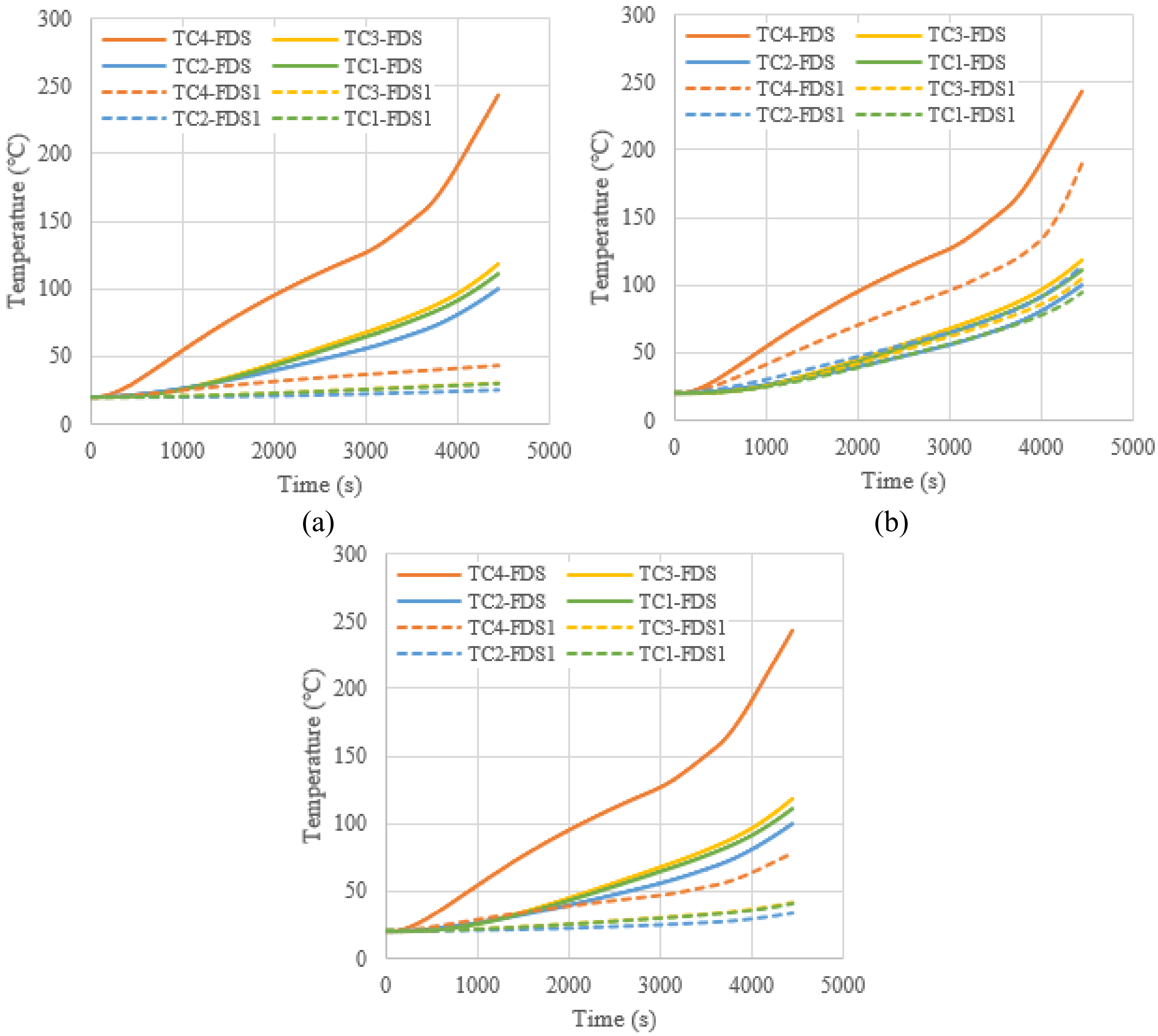

(a)

(b)

(c)

Figure 6.19 Different wind factors affecting the inside beam temperatures (a) Monin-Obukhov similarity theory (b) initial wind speed effect (c) ground level height effect.

Chapter 7 Conclusions

The present study establishes an FDS model of concrete beams subjected to channel fires to capture the gas and inside beam temperatures. The FDS model includes control volume and mesh, geometry and materials, fire load, and sensing devices. The experimental temperatures are compared with the predicted ones, and model uncertainties are quantified. The validated model is used to comprehensively investigate different parameters affecting the numerical temperatures. From these analyses, the following findings and conclusions are drawn.

- Generally, the predicted gas temperatures show good agreement with the test ones in different beams, and the simplified measured HRR can be used for modeling input.
- Most maximum and average temperature differences of each HRR plateau of the concrete beams range between -20% and 20%, which are acceptable in the experimental validation of fire engineering.
- From model uncertainty analysis, this model shows slightly higher numerical relative standard deviations than that in the Valencia Bridge fire tests (Alos-Moya et al. 2019) and McGrattan et al.'s study (McGrattan et al. 2013). However, the bias factors are much lower than that in other studies.
- From mesh sensitivity analysis, the optimal mesh size is identified. The effects of the computational zone, side hole area, burner surface temperature, measuring devices, and adiabatic surface on the temperatures are discussed from parametric studies.
- Moreover, one-dimensional heat conduction can be conducted for concrete beams withan air gap boundary condition for the back side of the layer in FDS. The predicted inside temperatures (each superposed from different surfaces) provide upper and lower limits for the experimental ones and the inside temperature near the fire shows the best

prediction. The surface layer thickness has significant effect, while the layer number does not affect predictions. The effect of specific heat and thermal conductivity on the inside temperatures are clarified.

- The wind effect is considered by the Monin-Obukhov similarity theory in FDS. Increasing initial wind speed and lowering ground level can decrease the inside beam temperatures. More well-controlled wind conditions should be recorded in future testing for further investigation and validation.

Although the present model shows promising gas and inside beam temperature predictions, a more refined geometrical model is still desirable. Inclined or circled obstructions can be established to refine the fire channel, especially the bottom region, and to include steel rebar in concrete beams.

References

Alos-Moya J, Paya-Zaforteza I, Garlock MEM, Loma-Ossorio E, Schiffner D, Hospitaler A, 2014. "Analysis of a bridge failure due to fire using computational fluid dynamics and finite element models." *Eng Struct* 68:96–110.

Alos-Moya J, Paya-Zaforteza I, Hospitaler A, Loma-Ossorio E, 2019. "Valencia bridge fire tests: Validation of simplified and advanced numerical approaches to model bridge fire scenarios." *Adv Eng Softw* 128:55–68.

C.S. Bajwa, E.P. Easton, H. Adkins, J. Cuta, N. Klymyshyn, S. Suffield, 2012. "The MacArthur Maze fire and roadway collapse: a 'worst case scenario' for spent nuclear fuel transportation?". in: Proceedings of the ASME 2012 Pressure Vessels & Piping Division Conference, Toronto, Ontario, Canada, 2012.

Dréan V, Girardin B, Chiva R, Guillaume E, Fateh T, 2022. "Numerical Investigation of the Thermal Exposure of Façade During BS 8414 Test Series: Influence of Wind and Fire Source." *Fire Technol.*

Dréan V, Schillinger R, Leborgne H, Auguin G, Guillaume E, 2018. "Numerical Simulation of Fire Exposed Façades Using LEPIR II Testing Facility." *Fire Technol* 54:943–66.

E. Aziz, V. Kodur, 2013. "An approach for evaluating the residual strength of fire exposed bridge girders." *J. Constr. Steel Res.* 88; 34–42.

E. Tonicello, S. Desanghere, O. Vassart, J.-M. Franssen, 2012. "Fire analysis of a new steel bridge." in: Proceedings of the 7th International Conference on Structures in Fire, Zurich, Switzerland, 2012.

Gong X, Agrawal AK, 2015. "Numerical Simulation of Fire Damage to a Long-Span Truss Bridge." *J Bridg Eng* 20:1–16.

I. Paya-Zaforteza, M.E.M. Garlock, 2012. "A numerical investigation on the fire response of a steel girder bridge." *J. Constr. Steel Res.* 75; 93–103.

J. Choi, 2008. "Concurrent Fire Dynamics Models and Thermomechanical Analysis of Steel and Concrete Structures." (Ph.D. dissertation), Georgia Institute of Technology, Atlanta, GA.

J.C. Dotreppe, S. Majkut, J.-M. Franssen, 2005. "Failure of a tied-arch bridge subjected to a severe localized fire." in: Proceedings of the 2005 IABSE Symposium, Lisbon, Portugal.

McGrattan K, Hostikka S, McDermott R, Floyd J, Weinschenk C, Overholt K, 2013a. "Fire dynamics simulator technical reference guide. Volume 1: mathematical model (version 6)." Gaithersburg, MD, USA: NIST Special Publication 1018.

McGrattan K, Hostikka S, McDermott R, Floyd J, Weinschenk C, Overholt K, 2013b. "Fire dynamics simulator user's guide (version 6)." User's guide. Gaithersburg, MD, USA: NIST Special Publication 1019.

McGrattan K, Hostikka S, McDermott R, Floyd J, Weinschenk C, Overholt K, 2013c. "Fire dynamics simulator technical reference guide. Volume 3: validation (version 6)." Gaithersburg, MD, USA: NIST Special Publication 1018-3.

McGrattan K, Steward Miles S, 2016. "Modeling fires using computational fluid dynamics (CFD). Chapter 32." SFPE handbook of fire protection engineering. 5th ed New York: Springer. p. 1034–65.

McGrattan K, Toman B, 2011. "Quantifying the predictive uncertainty of complex numerical models." *Metrologia* 48:173–80.

Peris-Sayol G, Paya-Zaforteza I, Alos-Moya J, Hospitaler A, 2015. "Analysis of the influence of geometric, modeling and environmental parameters on the fire response of steel bridges subjected to realistic fire scenarios." *Comput Struct* 158:333–45.

Quiel SE, Yokoyama T, Bregman LS, Mueller KA, Marjanishvili SM, 2015. "A streamlined framework for calculating the response of steel-supported bridges to open-air tanker truck fires." *Fire Saf J* 73:63–75.

Thunderhead Engineering, 2022. Pyrosim User Manual. Included in Pyrosim version 2022.2.0803.

Timilsina S, Yazdani N, Beneberu E, 2021. "Post-fire analysis and numerical modeling of a fire-damaged concrete bridge." *Eng Struct* 244:112764.

V. Kodur, E. Aziz, M. Dwaikat, 2013. "Evaluating fire resistance of steel girders in bridges." *J. Bridge Eng* 18; 633–643.

W. Wright, B. Lattimer, M. Woodworth, M. Nahid, E. Sotelino, 2013. "NCHRP Project No. 12-85: Highway Bridge Fire Hazard Assessment." Transportation Research Board of the National Academies, Washington, DC, 2013.

Y. Bao, M.S. Hoehler, C.M. Smith, M. Bundy, G. Chen, 2017. "Temperature measurement and damage detection in concrete beams exposed to fire using PPP-BOTDA based fiber optic sensors." *Smart Mater. Struct*. 26 (8), p. 105034.

Y. Liu, W. Guangyuan, S. Yansheng, 2012. "Finite element analysis of fire behavior of steel girders in bridges." *Adv. Mater. Res.* 594–597; 2296–2300.